Naval Surface Warfare Center
Indian Head Division
Indian Head, MD 20640-5150

IHTR-2022-004048
August 16, 2022

Effects of Electric Fields on High Explosives as Determined by Density Functional Theory

Alexander S. Hyla, Ph.D.

This page intentionally left blank

REPORT DOCUMENTATION PAGE

Form Approved
OMB No. 0704-0188

1. REPORT DATE *(DD-MM-YYYY)*	2. REPORT TYPE	3. DATES COVERED *(From - To)*
16-08-2022	Technical Report	01 OCT 2020 – 30 SEP 2021

4. TITLE AND SUBTITLE

Effects of Electric Fields on High Explosives as Determined by Density Functional Theory

5a. CONTRACT NUMBER

5b. GRANT NUMBER

5c. PROGRAM ELEMENT NUMBER

6. AUTHOR(S)

Alexander S. Hyla, Ph.D.

5d. PROJECT NUMBER

5e. TASK NUMBER

5f. WORK UNIT NUMBER

7. PERFORMING ORGANIZATION NAME(S) AND ADDRESS(ES)

Naval Surface Warfare Center Indian Head Division
Indian Head, MD 20640-5150

8. PERFORMING ORGANIZATION REPORT NUMBER

IHTR-2022-004048

9. SPONSORING/MONITORING AGENCY NAME(S) AND ADDRESS(ES)

Kerry Clark NSWC IHD and Office of Naval Research

10. SPONSOR/MONITOR'S ACRONYM(S)

11. SPONSOR/MONITOR'S REPORT NUMBER(S)

12. DISTRIBUTION/AVAILABILITY STATEMENT

DISTRIBUTION STATEMENT A – Approved for Public Release (22-157): Distribution is Unlimited.

13. SUPPLEMENTARY NOTES

14. ABSTRACT

This report describes the changes that four representative molecular high explosives (HEs) undergo upon exposure to applied electric fields, as determined using density functional theory. The electric fields were varied in magnitude and orientation with respect to the molecule. Pictures will be presented that show changes in the optimized electron density due to the applied electric fields. These changes will enable better understanding of how electric fields can be used to start the process of HE decomposition. An example of the decomposition was looked at for each HE, namely the breaking of a bond to release $-NO_2$ from the molecule. These products were optimized both with and without applied electric fields as part of the process to obtain transition state geometries and energies to determine the effect of the applied electric field on the activation energy to decomposition, which is related to the sensitivity of the HEs.

15. SUBJECT TERMS

High explosive, Electric field, Density functional theory, RDX, PETN, TNT, TATB

16. SECURITY CLASSIFICATION OF:			17. LIMITATION OF ABSTRACT	18. NUMBER OF PAGES	19a. NAME OF RESPONSIBLE PERSON
a. REPORT	b. ABSTRACT	c. THIS PAGE			Alexander Hyla
U	U	U	None	62	19b. TELEPHONE NUMBER *(Include area code)* 301-744-1658

This page intentionally left blank.

FOREWORD

The goal of this work is to investigate the initial reactions of high explosives (HEs) and determine how these reactions would be affected by the application of external electric fields. Since many high explosives have molecular moments, such as dipole or quadrupole moments, they are dielectric materials and can be polarized by electric fields. It is not well known at the molecular level how HEs will respond to external electric field perturbations, but other dielectric molecules have shown changes in electron density. This change in electron density appears as changes in bond lengths and bond angles following similar insults, which suggests that some bonds may become easier or harder to break, depending on the insult. These electric field insults may provide some control over the HE's sensitivity. In order to accomplish this goal, density functional theory calculations were used to study how representatives of four different types of HE molecules initially behave without any applied electric fields and following the electric field insult. The first step in the decomposition of these particular HEs was the removal of a $–NO_2$ group and that process was studied to determine how the direction and magnitude of the applied electric field may affect this initial reaction of decomposition. These four different HEs showed differences in how the removal of $–NO_2$ occurs under applied electric fields, suggesting that there is an effect of electric fields to control the sensitivity of certain HEs. The next steps are to look into the effect of HE intermolecular interactions to determine how the bulk material may respond to electric field insults, how ingredients used in propellants and other applications may be influenced by applied electric fields, and how these HE changes due to electric field insults may lead to changes in the interactions with the other ingredients used in desired applications.

This work was performed as a part of an In-house Laboratory Independent Research (ILIR) Project at Naval Surface Warfare Center Indian Head Division. The author would like to thank Drs. Gerardo Pangilinan, Sunil Dwivedi, and Vasant Joshi (all from NSWC IHD) for their time, valuable comments, and help in improving this report.

Approved and released by:

DWIVEDI.SUNIL.KUMAR.1508230172 Digitally signed by DWIVEDI.SUNIL.KUMAR.1508230172 Date: 2022.10.13 11:49:57 -04'00'

Dr. Sunil Dwivedi, Senior Technical Lead for Modeling and Simulation — 10/13/2022 Date

GRIEVE.ALAN.1505446646 Digitally signed by GRIEVE.ALAN.1505446646 Date: 2022.10.25 16:12:30 -04'00'

Dr. Alan Grieve, R13 Materials Science Branch Manager — 10/25/2022 Date

This page intentionally left blank**.**

EXECUTIVE SUMMARY

This report describes the changes that four representative molecular high explosives (HEs) undergo upon exposure to applied electric fields, as determined using density functional theory. The electric fields were varied in magnitude and orientation with respect to the molecule. Results are presented that show changes in the optimized electron density due to the applied electric fields. These changes help understand how electric fields can be used to initiate the process of HE decomposition. An example of the decomposition is presented for each HE, namely the breaking of a bond to release $–NO_2$ from the molecule. These products were optimized both with and without applied electric fields as part of the process to obtain transition state geometries and energies to determine the effect of the applied electric field on the activation energy to decomposition, which is related to the sensitivity of the HEs.

This page intentionally left blank**.**

CONTENTS

Heading *Page*

Tables

Figures

This page intentionally left blank.

ACRONYMS AND ABBREVIATIONS

Å	Angstrom = 10^{-10} meters
aug-cc-pVDZ	Augmented correlation-consistent polarized basis set with double zeta description of valence electrons
aug-cc-pVTZ	Augmented correlation-consistent polarized basis set with triple zeta description of valence electrons
a.u.	Atomic units
B3LYP	Hybrid Becke 3 parameter exchange density functional with Lee-Yang-Parr correlation density functional with 20 % exact Hartree-Fock exchange
D	Debye = 3.336×10^{-30} Coulomb·meter
D3BJ	Grimme's third empirical dispersion correction with Becke-Johnson damping
DFT	Density functional theory
|e|	Magnitude of the charge of an electron
HE	High explosive
K	Kelvin
PETN	2,2-Bis[(nitrooxy)methyl]propane-1,3-diyl dinitrate
RDX	1,3,5-Trinitro-1,3,5-triazinane
TATB	2,4,6-Trinitrobenzene-1,3,5-triamine
TNT	2-Methyl-1,3,5-trintirobenzene
V/m	Volts per meter
Ψ	Wavefunction

This page intentionally left blank.

EFFECTS OF ELECTRIC FIELDS ON HIGH EXPLOSIVES AS DETERMINED BY DENSITY FUNCTIONAL THEORY

Overview

This report describes the changes that four representative molecular high explosives (HEs) undergo upon exposure to applied electric fields, as determined using density functional theory (DFT). The electric fields were varied in magnitude and orientation with respect to the molecule. Results are presented that show changes in the optimized electron density due to the applied electric fields. These changes help understand how electric fields can be used to initiate the process of HE decomposition. An example of the decomposition is presented for each HE, namely the breaking of a bond to release $–NO_2$ from the molecule. These products were optimized both with and without applied electric fields as part of the process to obtain transition state geometries and energies to determine the effect of the applied electric field on the activation energy to decomposition, which is related to the sensitivity of the HEs. Molecular dipole moments, due to electric field-induced geometrical changes, are also presented.

Introduction

The motivation for looking at calculations with applied electric fields comes from the desire to understand and exploit the response of materials, particularly dielectric materials, to applied electromagnetic radiation. These materials can be used to create switchable propellants, where applying a potential can cause a change in the material which leads to ignition of the propellant and removing the potential will extinguish the propellant. In order to accomplish this goal, density functional theory will be used to perform these calculations.

Density functional theory was developed in the 1960s by Hohenberg and Kohn who found a direct relationship between the electron density and the wavefunction which describes where electrons are likely located in space [1]. This theory uses the electron density in order to solve the Schrödinger equation ($\widehat{H}\Psi = E\Psi$). By minimizing the electron density, the ground state electron configuration (and thus the geometry) can be obtained. This method is much less computationally expensive than the wavefunction-based methods used previously (going from 3N degrees of freedom, where N is the number of atoms in the system, to only three). DFT is not only computationally faster than wavefunction-based methods, but it can be almost as accurate, with judicious choices of the parameters required for calculations. DFT is a useful tool for determining the geometries and energies of systems with a good balance of computational effort and accuracy. It is this balance of accuracy and computational effort that led to the use of DFT for calculating the effect of applied electric fields on the changes in electron density and geometry for the systems of interest. Since DFT is known to give fairly accurate geometries, comparable to experimental data, it was chosen to study the ground state of the unperturbed HE molecules. Without a proper description of the unperturbed ground states as frames of reference, one cannot determine the effects of the perturbations, here an electric field, or give suggestions of what is occurring in real life applications from the calculated results.

This project required optimizing the structure of molecules under applied electric fields to determine how their electron density changed. By understanding the change of the electron density by the magnitude and direction of the applied electric field, a database of responses can be created for different applications, such as remote sensing of materials, dielectric ignitors, or switchable propellants. By matching the response of a material in a device, such as an IED, the type of explosive may be matched to the database and help defeat this threat. Dielectric ignitors are dielectric materials which can be inserted into a formulation, such as a propellant, and when electromagnetic radiation is applied, they absorb the radiation and heat up enough to ignite the HE. Switchable propellants involve applying a potential which leads to a change in the molecular or electronic structure of a portion of the propellant (maybe just an additive or a binder or the entire formulation) which causes ignition while removing the potential extinguishes the propellant. Switchable propellants can increase the range of devices by allowing for non-

continuous burning and coasting periods, such as rockets and missiles, which use this propellant, and can be used for terminal effects.

In this study, four HEs were chosen to represent different types of HEs. 1,3,5-Trinitro-1,3,5-triazinane (RDX) was chosen to represent nitramine HEs. 2-Methyl-1,3,5-trintirobenzene (TNT) was used to represent nitroarene HEs. 2,4,6-Trinitrobenzene-1,3,5-triamine (TATB) was chosen to represent aromatic nitroaniline HEs. 2,2-Bis[(nitrooxy)methyl]propane-1,3-diyl dinitrate (PETN) was chosen to represent nitrate ester HEs. The chemical structures, abbreviations, and HE type for these 4 molecules are shown in Figure Figure 1.

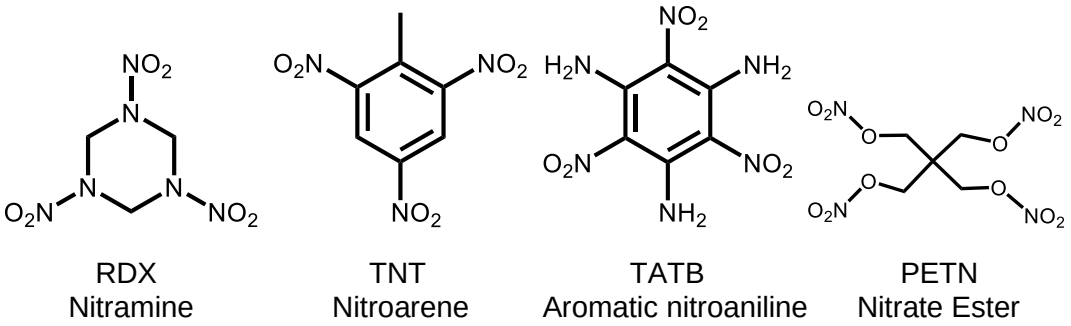

Figure 1. Chemical structures of the high explosives used in this study. The abbreviated name and the type of high explosive are below the chemical structures.

Assumptions

In order to complete the calculations which were used to prepare the data and results used in this report, a few assumptions had to be made at the start. By using DFT, there are a few implicit assumptions, such as the Born-Oppenheimer approximation, which says that due to the large mass difference between electrons and the particles that make up the nucleus, the electron movement can be decoupled from nuclear movement. Another assumption was that the exact functional form of the exchange-correlation functional is not known and the DFT methods used were approximations to this exact exchange-correlation functional. DFT calculations also assumed that the temperature of the calculations was 0 K. Temperature corrections can be performed, but they are not included by default.

These calculations involve only a single HE molecule in a vacuum. Since the initial atomic positions were taken from experimental crystal structures, it was assumed that the energy minimization routine performed in the quantum mechanical program led to the ground state of the molecule and not a meta-stable, transition point. Confirmation that the structures were energy minima was obtained by completing a frequency analysis and ensuring that there were no imaginary (negative) frequencies. The DFT optimized geometries were compared to crystal structure data and it was assumed that if the ground state of the HEs could be represented well by the DFT methodology/level of theory, then the DFT determined geometries and energy levels would be well represented when the HEs were insulted by applied electric fields. For this study, the effects of intermolecular interactions were not included due to increases in the required computational resources. It was also assumed that the quantum mechanical program's treatment of the electric field accurately describes the true interaction of molecules with applied electromagnetic radiation. It was also assumed that the applied electric field would impact the geometry and energy levels of the HEs, which may have an influence on the decomposition of the HE toward initiation.

In order to look at the potential decomposition products, it was assumed that the most commonly reported mechanisms held true for the decomposition of these HEs. Using this assumption, one NO_2 group was removed from the HE molecule to a distance that was assumed to discourage bonding interactions from occurring with the rest of the molecule and this structure with a free NO_2 group was used to optimize the geometry. After the

calculations were finished, it was determined that this initial distance was not sufficient for certain HEs to discourage bonding between the removed NO_2 group and the rest of the HE molecule.

Methodology

All calculations presented in this technical report were completed using the Gaussian 16 computational chemistry program (Gaussian 16 revision C.01) [2]. Visualizations were made using GaussView 6 [3]. Molecular structures were prepared using the ChemDraw program.

Initially, the four HEs were geometry optimized using the B3LYP-D3BJ/aug-cc-pVTZ level of density functional theory (DFT) [4-6]. B3LYP-D3BJ/aug-cc-pVTZ is the compact way to say that the DFT level of theory consisted of the B3LYP hybrid functional [4] combined with the D3BJ dispersion correction [5] while using the aug-cc-pVTZ basis set [6]. After the initial optimization, it was determined that the TATB molecule was not going to converge self-consistently at this level of theory, so the smaller aug-cc-pVDZ basis set was chosen with the same B3LYP-D3BJ functional as the next option and self-consistent convergence was reached. Frequency analysis was performed to ensure that there were no imaginary (negative) frequencies for the optimized structures, which ensured that the structure was a minimum on the potential energy surface and not a saddle point. Once the four HEs were optimized, static electric fields of varying magnitude and alignment with respect to the molecular orientation were applied to the optimized geometry and the system was allowed to re-optimize the geometry and energies in the electric field, using the same level of theory as the initial optimization without electric fields. The magnitudes of the electric fields were varied from 5.1×10^7 V/m to 2.6×10^{10} V/m (2.6 V/Å). These electric fields were somewhat stronger than those observed at the dielectric breakdown of composite explosives (~1 - 4 $\times 10^7$ V/m) [7], but were on the same order of magnitude as the fields observed at the interface of two materials, particularly core-shell metal nanoparticles (~10^9 V/m) [8]. Frequency analysis was again performed on each optimized structure to determine that the structures were minimum structures on the potential energy surface. Gaussian cube files were prepared of the electron density using the "formchk" and "cubegen" programs built in with the Gaussian 16 program. The cube files were used to visualize the electron density using the GaussView 6 program. The effect of applied electric fields can be seen on the changes in geometry of TATB in Figure 2 below.

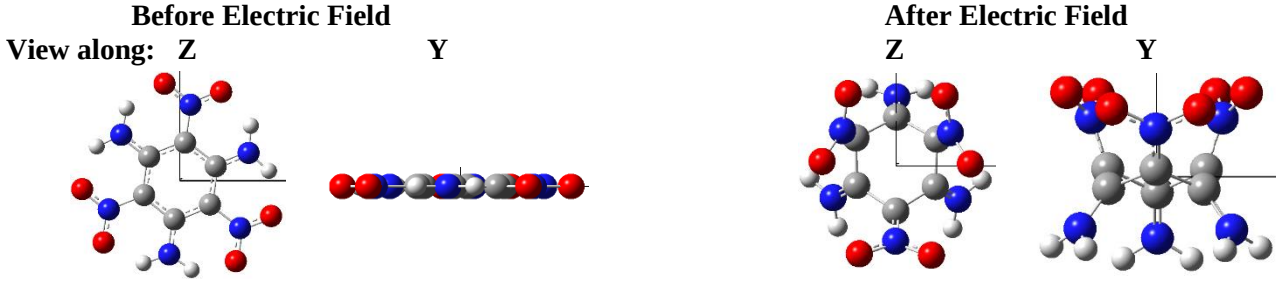

Figure 2. Optimized geometries of TATB before (left) and after (right) interaction with an electric field applied along the z-molecular axis (out of the plane of the benzene ring). The views are along the z axis (left of each side) and along the y axis (right of each side). Carbon atoms are gray, oxygen atoms are red, nitrogen atoms are blue and hydrogen atoms are white.

To examine a product of HE decomposition, the R-NO_2 bond (R = C, N, O) was artificially extended to 1.5 Å longer than the optimized bond length (1.5 Å was about the distance of the optimized R-N bond lengths), which resulted in distances of at least 2.7 Å. Each of the R-NO_2 bonds were separately extended in the HEs (for each molecule only one bond was lengthened and the others remained the same as the optimized geometry). This created 3 (RDX, TNT, TATB) or 4 (PETN) different geometries of the decomposition products for the HE molecules in the study, so that the effect of the different magnitudes and orientations of the applied electric fields with respect to the molecule could be determined on these different geometries. The different geometries were then optimized without

any applied electric fields to use as the baseline for any changes caused by the applied electric fields. A free nitro group was expected in these optimized structures. The B3LYP-D3BJ/aug-cc-PVTZ level of theory was used for the RDX, TNT, and PETN molecules, while the B3LYP-D3BJ/aug-cc-pVDZ level of theory was used for the TATB molecule, as used for the initial geometry optimizations. The TNT and TATB calculations using the decomposition products as the input geometry optimized, but they optimized to structures without free nitro groups (all nitro groups were bound).

Results and Discussion

Ground State Optimization

The ground state geometries and electron configurations of the four representative HEs were optimized using DFT at the B3LYP-D3BJ/aug-cc-pVTZ (RDX, TNT, PETN) or aug-cc-pVDZ (TATB) level without any applied electric fields. These optimized geometries were compared to the crystal structures of the HEs to determine how well this level of theory described the experimental geometrical values, such as bond lengths, angles, and dihedrals [9-12]. The B3LYP-D3BJ/aug-cc-pVTZ level of theory optimized the bonds of TNT to within 1 % of the crystal structure values, while the largest deviations in bond length for RDX and PETN were within 5 ± 1 %. The angles for RDX, TNT, and PETN were optimized to within 5 % of those values determined from crystal structures. The B3LYP-D3BJ/aug-cc-pVDZ level of theory had some trouble optimizing N-H bonds present in TATB, and due to the overestimation of these bond lengths, the maximum error in bond lengths compared to crystal structure data was around 27 %. The angles obtained through DFT calculations were less than 10 % different than those obtained from the crystal structure of TATB. Figure 3 shows the geometry of PETN as viewed from the molecular x, y, and z-axes, along with the optimized electron densities viewed along these axes. The electron densities show the surface in space at which there is 0.0004 $|e|/Å^3$ or larger inside this surface. This is the environment that other molecules or perturbations would see and interact with in space.

Optimization of Ground State with Applied Electric Fields

Once the ground state geometries of the HEs were optimized, an electric field was applied and the HEs were allowed to relax in the electric field during a second geometry optimization. This relaxation was to allow for the interaction of the electric field with the electron density of the molecule. Due to the anisotropic nature of the HE geometries, the electric field was applied along different molecular directions. This allowed for different parts of the molecule to interact with the electric field. The fields were applied along the molecular x-, y-, and z-axes and the original configuration was oriented to have the molecule lying in the xy-plane, if possible, or at least oriented so the major axis of the molecule was parallel to the xy-plane. The magnitude of the electric field was also varied to see how the intensity changed the interaction with the HEs. The magnitude was varied from 0 V/m to 2.6×10^{10} V/m (2.6 V/Å). When the electric field was strong enough, the electron density rearranged to a lower energy configuration, which resulted in changes in bond lengths, bond angles, dipole moments, and electron density maps. Images of the electron density following interaction with the applied electric field can be found in Figures 4 – 15. Figures Figure 4 – Figure 6 show the electron densities of the RDX in response to applied electric fields in different directions. Figures Figure 7 – Figure 9 show the responses of the electron density of TNT to the applied electric fields. The electron density responses of TATB can be found in Figures Figure 10 – Figure 12 and PETN electron density responses to applied electric fields are shown in Figures Figure 13 – Figure 15. The changes in dipole moment due to the electric field-induced geometrical changes are summarized in Tables Table II – Table V.

RDX had major changes to the electron density at different electric field intensities along different molecular axes (Table I). When the electric field was applied along the RDX molecular x-axis, Figure 4 showed that there was a major change in the geometry and corresponding shape of the electron density at 2.6×10^9 V/m. However, when the field was applied along the RDX molecular y-axis (Figure 5), the geometry and electron density remained fairly stable up to the largest magnitude tested (5.1×10^9 V/m). Applying an electric field along the RDX molecular z-axis (Figure 6) had a major change in the geometry and corresponding shape of the electron density at

2.6×10^9 V/m. A similar pattern was seen with electric fields applied along the TNT molecular x- and y-axes. An electric field along the x-axis (Figure 7) showed a noticeable change in the geometry and electron density map at a magnitude of 5.1×10^9 V/m, while there was no change in the general shape of the electron density map at this same electric field magnitude, but along the molecular y-axis (Figure 8). The electron density map and geometry changed when the electric field was applied along the TNT molecular z-axis at the magnitude of 5.1×10^9 V/m (Figure 9) because a nitro group moved towards larger z values following the applied electric field.

The dipole moment of RDX also changed anisotropically, just as the geometry, with both the magnitude and the orientation of the applied electric field (Table II). In all cases studied for RDX, the dipole moment was found to only be along the molecular z-axis. The dipole moments monotonically increased as the magnitude of the electric field increased along each of the molecular x-, y-, and z-axes, but the values of the dipole moments differed with the orientation of the electric field. When the field was applied along the x-direction, the largest magnitude (5.1×10^9 V/m) led to a dipole moment of 7.29 D, whereas the same magnitude of field applied along the y- and z-axes resulted in dipole moments of 7.41 D and 10.41 D, respectively. These dipole moments are rather large, which typically indicates ionic type, or charge transfer, character. The dipole moment from the z-axis applied field is on the order of the dipole moment found in KBr (10.6 D). [13]

The dipole moments of TNT (Table III) were similar to RDX, in that they changed anisotropically, but the dipole moments from the geometries obtained with an electric field applied along the y-axis began decreasing as the magnitude increased (1.66 D to 0.71 D), until it sharply increased to 3.03 D at the largest magnitude (5.1×10^9 V/m). The dipole moments of the molecules with electric fields applied along the x- and z-axes monotonically increased, but the magnitudes of the dipole moment was not as large as those seen in RDX.

PETN was different from RDX and TNT, because the electric fields applied along each of the three molecular axes led to changes in geometry and electron density. The electric fields along the PETN molecular x- and y-axes caused major changes to the geometries and electron densities at the same magnitude of 5.1×10^9 V/m (see Figures Figure 13 and Figure 14). The nitro groups tended to be more strongly affected by the electric field than the rest of the PETN molecule. The nitro groups were moved along the direction of the applied electric field. When the electric field was applied along the PETN molecular z-axis, the magnitude of 5.1×10^9 V/m was sufficient enough to cause large changes in geometry and the corresponding electron density (Figure 15). This was caused by the rotation and translation of nitro groups to align with the applied electric field in the z-direction.

The dipole moments of PETN (Table V) were similar to those of TNT, where one direction of electric field application led to a decrease in the dipole moment of the system as the electric field magnitude increased, before increasing at higher electric field magnitudes. For PETN, the dipole moments of the molecules with an electric field applied along the molecular z-axis decreased from 1.61 D at 0 V/m to 1.13 D at 5.1×10^8 V/m, before increasing to 3.83 D and 6.07 D at 2.6×10^9 V/m and 5.1×10^9 V/m, respectively. Applying electric fields along the molecular x- and y-axes of PETN led to dipole moments that monotonically increased with values slightly larger than those seen in RDX (along the x-direction: 8.81 D for PETN, 7.29 D for RDX, along the y-direction: 8.41 D for PETN, 7.41 D for RDX).

TATB was a special case in that it was the only molecule in the study that did not converge at the same B3LYP-D3BJ/aug-cc-pVTZ level as the other HEs. The smaller aug-cc-pVDZ basis set was used to obtain convergence and this means that the results for TATB cannot be compared directly to the other HEs in this study. TATB only underwent some twisting out of planarity at electric fields with large magnitudes (at least 5.1×10^9 V/m) in the molecular y- and z-directions (Figures Figure 11-Figure 12). At the electric field magnitudes tested along the x-direction (Figure 10), there was no major twisting of the TATB molecule. Calculations with an electric field magnitude of 2.6×10^{10} V/m applied along the z-axis led to a breaking of planarity in the benzene ring portion of the TATB molecule. The resulting geometry had C-C bond lengths similar to a cyclohexane chair configuration and all of the nitro groups pointing in the same direction (upward in Figure Figure 12) while the amino groups were pointing in the other direction (downward in Figure Figure 12).

The dipole moments for TATB (Table IV) are similar to those for RDX, in that they monotonically increase with the magnitude of the electric field for all orientations. However, since these results were obtained with a

different basis set than the other three HEs, they must be considered by themselves. The dipole moment with no applied electric field is negligible, but it starts to increase and has values in the order of TNT and PETN around the same electric field magnitudes (2.6×10^9 V/m). The TATB molecule was able to be optimized with an electric field applied along the molecular z-direction which had the largest magnitude field in this study. This very large electric field magnitude (2.6×10^{10} V/m) led to a dipole moment of 45.74 D, which was due to the large distance between the nitro groups and the amino groups created when the planar TATB became cyclohexane like, with all of the amino groups pointing one direction and the amino groups pointing in the opposite direction.

Table I. Voltage of Applied Electric Fields at Which Noticeable Change First Appeared in the Geometry and Electron Density in Different Molecular Directions. All units are V/m.

Electric field applied along	RDX	TNT	TATB	PETN
X axis	2.6×10^9	5.1×10^9	NA [b]	5.1×10^9
Y axis	NA [a]	NA [a]	5.1×10^9	5.1×10^9
Z axis	5.1×10^9	5.1×10^9	5.1×10^9	5.1×10^9

[a] Largest electric field magnitude studied was 5.1×10^9 V/m. [b] Largest electric field magnitude studied was 2.6×10^9 V/m.

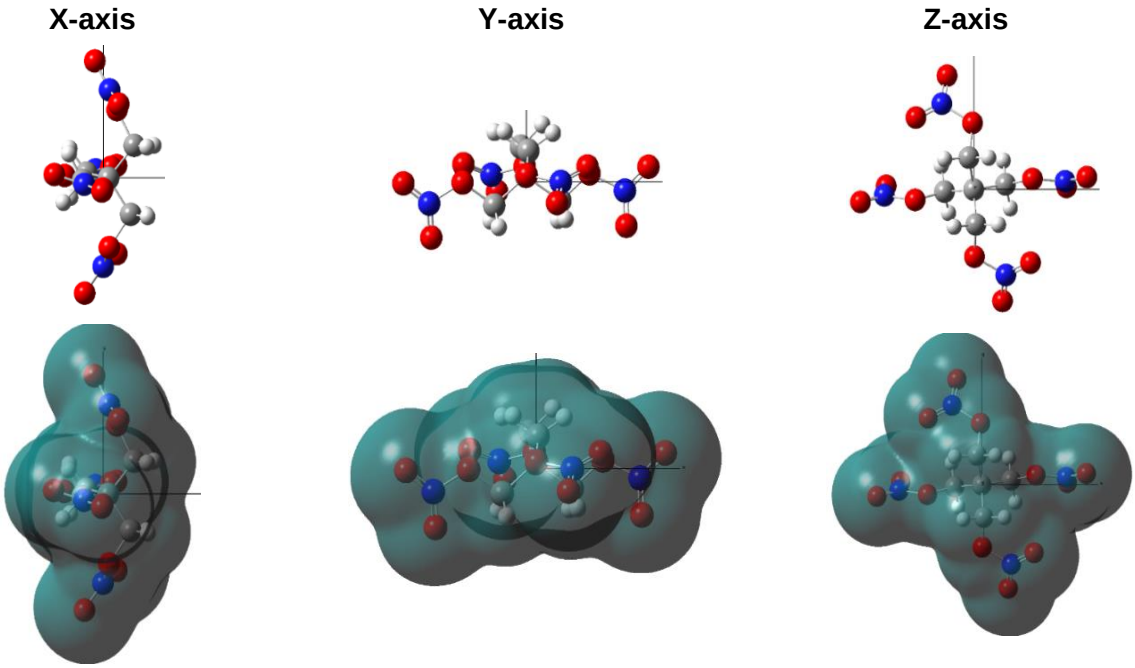

Figure 3. Optimized geometry (top) and optimized electron density (bottom) of PETN at the B3LYP-D3BJ/aug-cc-pVTZ level of theory viewed from the molecular x-axis, y-axis, and z-axis. The isosurface value of the electron densities is 0.0004 |e|/Å³. Carbon atoms are gray, oxygen atoms are red, nitrogen atoms are blue and hydrogen atoms are white.

Table II. Dipole Moments of the Optimized Geometries of RDX Both With and Without Applied Electric Fields. All units are D.[a]

Electric field applied along	0 V/m	5.1×10^7 V/m	2.6×10^8 V/m	5.1×10^8 V/m	2.6×10^9 V/m	5.1×10^9 V/m
X axis	3.19	3.19	3.22	3.29	5.23	7.29
Y axis	3.19	3.23	3.39	3.60	5.27	7.41
Z axis	3.19	3.19	3.22	3.27	3.99	10.41

[a] All calculated dipole moments were found to only lie along the molecular z-axis. Therefore, the calculated total dipole moment will be presented.

Table III. Dipole Moments of the Optimized Geometries of TNT Both With and Without Applied Electric Fields. All units are D.[a]

Electric field applied along	0 V/m	5.1×10^7 V/m	2.6×10^8 V/m	5.1×10^8 V/m	2.6×10^9 V/m	5.1×10^9 V/m
X axis	1.66	1.66	1.66	1.70	2.81	4.92
Y axis	1.66	1.61	1.42	1.19	0.71	3.03
Z axis	1.66	1.66	1.66	1.67	2.20	3.57

[a] All calculated dipole moments were found to only lie along the molecular z-axis. Therefore, the calculated total dipole moment will be presented.

Table IV. Dipole Moments of the Optimized Geometries of TATB Both With and Without Applied Electric Fields. All units are D.[a]

Electric field applied along	0 V/m	5.1×10^7 V/m	2.6×10^8 V/m	5.1×10^8 V/m	2.6×10^9 V/m	5.1×10^9 V/m	2.6×10^{10} V/m
X axis	5.14×10^{-4}	0.07	0.34	0.67	3.33	NA	NA
Y axis	5.14×10^{-4}	0.07	0.32	0.67	3.28	6.50	NA
Z axis	5.14×10^{-4}	0.04	0.18	0.37	1.87	3.91	45.74

[a] All calculated dipole moments were found to only lie along the molecular z-axis. Therefore, the calculated total dipole moment will be presented.

Table V. Dipole Moments of the Optimized Geometries of PETN Both With and Without Applied Electric Fields. All units are D.[a]

Electric field applied along	0 V/m	5.1×10^7 V/m	2.6×10^8 V/m	5.1×10^8 V/m	2.6×10^9 V/m	5.1×10^9 V/m
X axis	1.61	1.61	1.65	1.78	3.97	8.81
Y axis	1.61	1.61	1.65	1.75	3.69	8.71
Z axis	1.61	1.56	1.37	1.13	3.83	6.07

[a] All calculated dipole moments were found to only lie along the molecular z-axis. Therefore, the calculated total dipole moment will be presented.

Electric Field (a.u.)	Electric Field (V/m)	View along X-direction	View along Y-direction	View along Z-direction
0	0	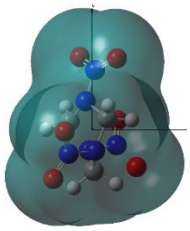	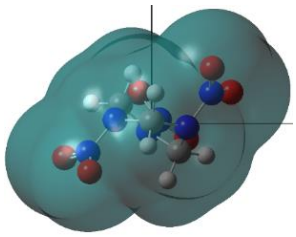	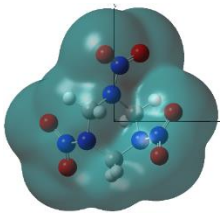
0.0001	5.1×10^7	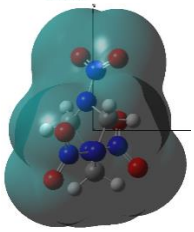	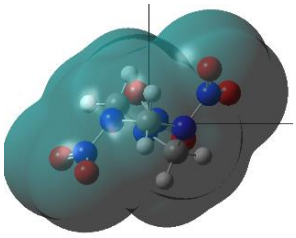	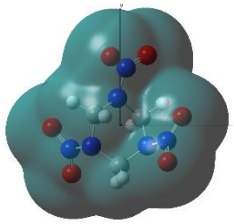
0.0005	2.6×10^8	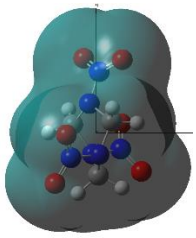	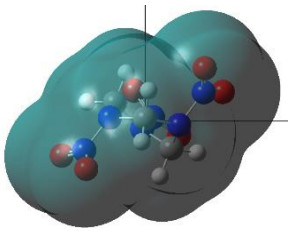	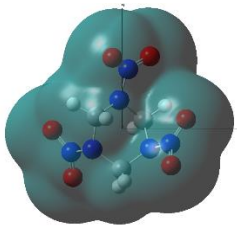
0.001	5.1×10^8	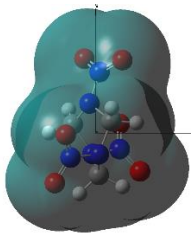	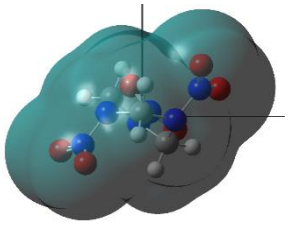	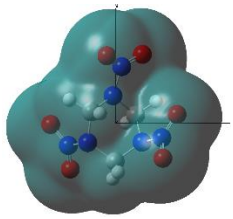
0.005	2.6×10^9	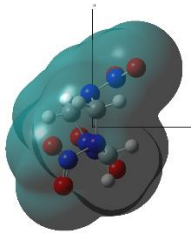	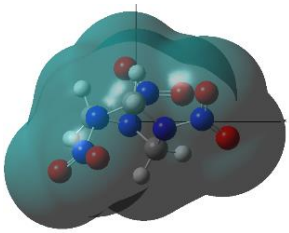	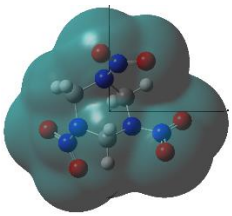
0.01	5.1×10^9	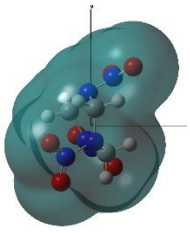	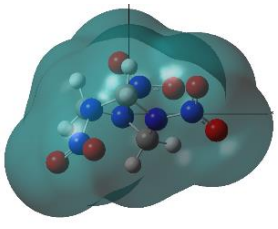	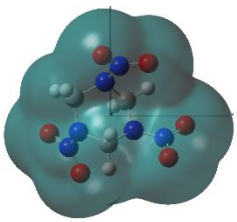

Figure 4. B3LYP-D3BJ/aug-cc-pVTZ optimized electron densities of RDX under an electric field applied along the x-direction viewed along x, y, and z directions. Isosurface values are 0.0004 $|e|/Å^3$.

Electric Field (a.u.)	Electric Field (V/m)	View along X-direction	View along Y-direction	View along Z-direction
0	0	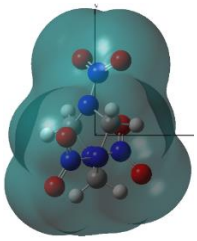	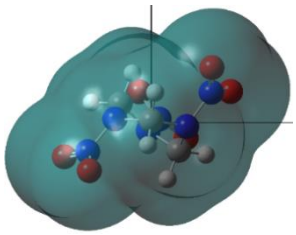	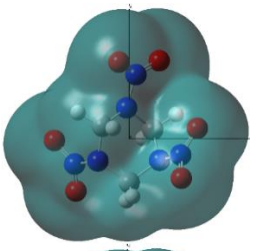
0.0001	5.1×10^7	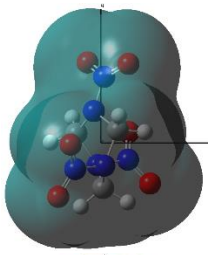	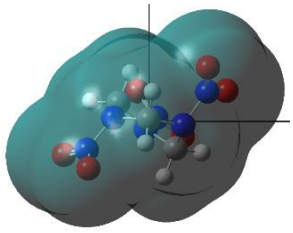	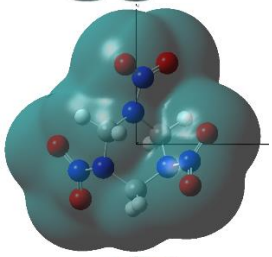
0.0005	2.6×10^8	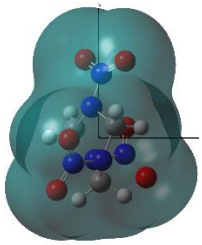	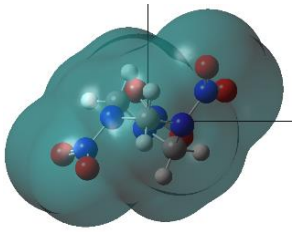	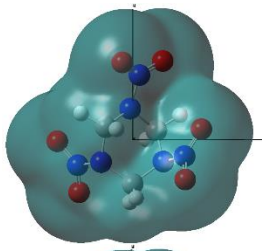
0.001	5.1×10^8	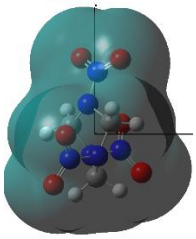	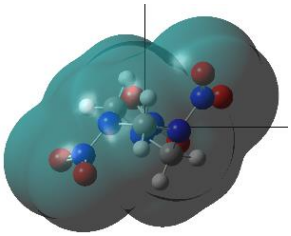	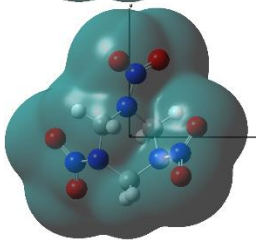
0.005	2.6×10^9	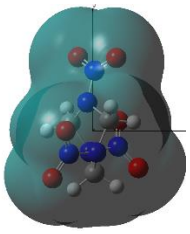	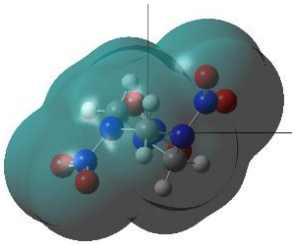	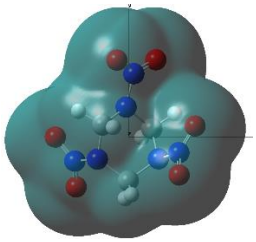
0.01	5.1×10^9	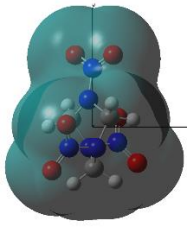	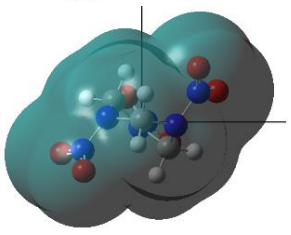	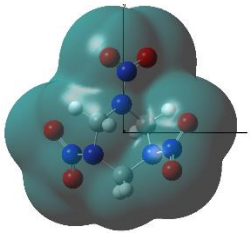

Figure 5. B3LYP-D3BJ/aug-cc-pVTZ optimized electron densities of RDX under an electric field applied along the y-direction viewed along x, y, and z directions. Isosurface values are 0.0004 $|e|/Å^3$.

Electric Field (a.u.)	Electric Field (V/m)	View along X-direction	View along Y-direction	View along Z-direction
0	0	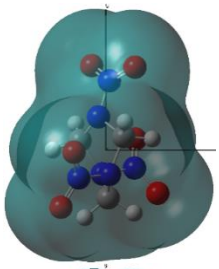	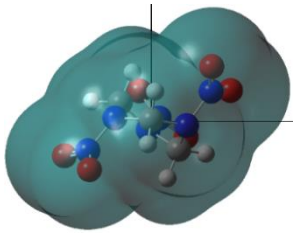	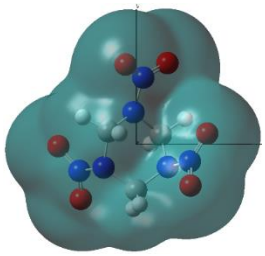
0.0001	5.1×10^{7}	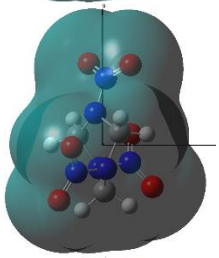	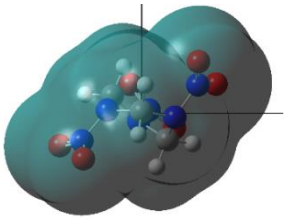	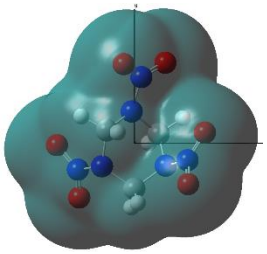
0.0005	2.6×10^{8}	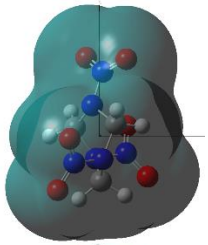	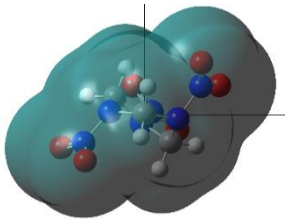	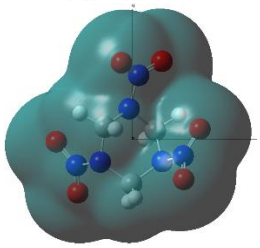
0.001	5.1×10^{8}	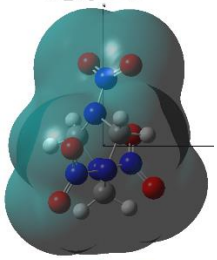	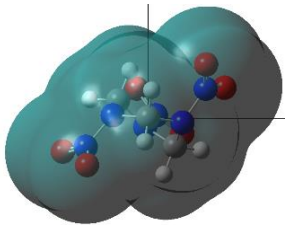	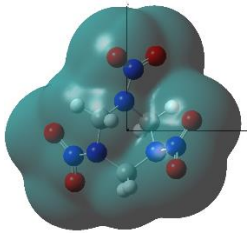
0.005	2.6×10^{9}	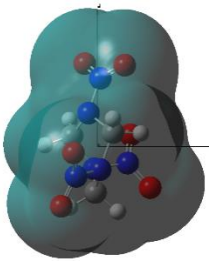	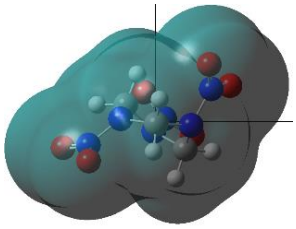	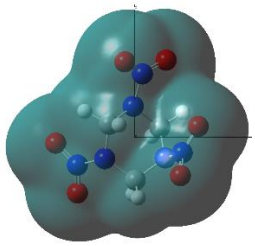
0.01	5.1×10^{9}	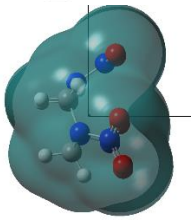	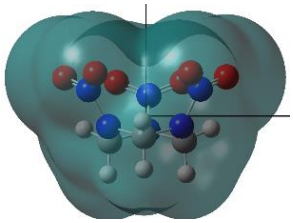	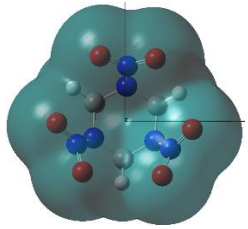

Figure 6. B3LYP-D3BJ/aug-cc-pVTZ optimized electron densities of RDX under an electric field applied along the z-direction viewed along x, y, and z directions. Isosurface values are 0.0004 $|e|/Å^3$.

Electric Field (a.u.)	Electric Field (V/m)	View along X-direction	View along Y-direction	View along Z-direction
0	0	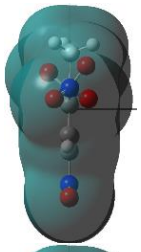	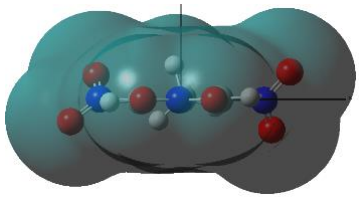	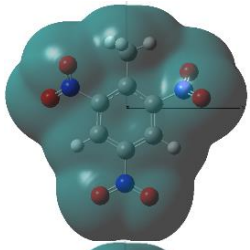
0.0001	5.1×10^{7}	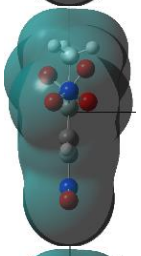	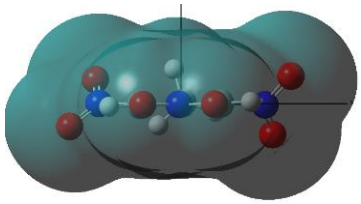	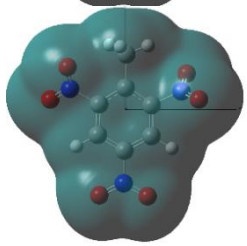
0.0005	2.6×10^{8}	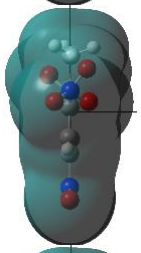	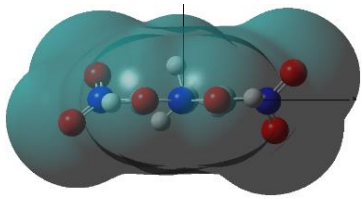	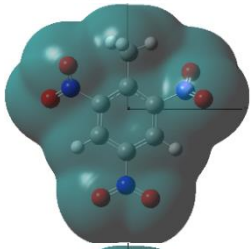
0.001	5.1×10^{8}	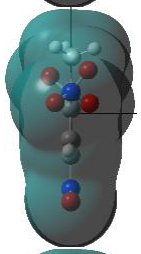	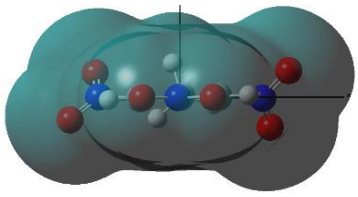	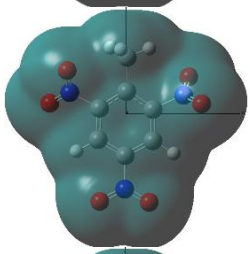
0.005	2.6×10^{9}	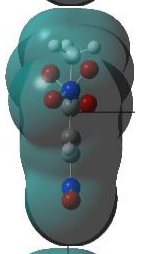	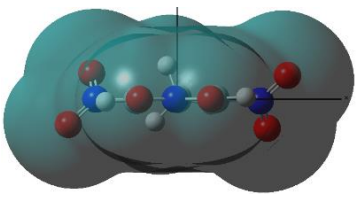	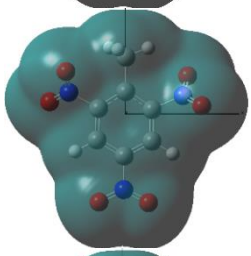
0.01	5.1×10^{9}	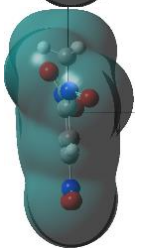	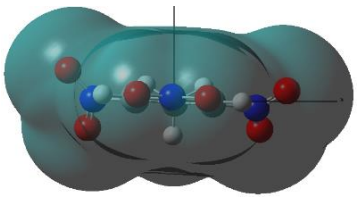	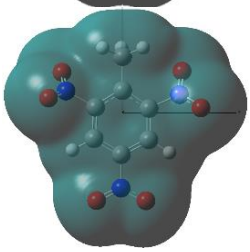

Figure 7. B3LYP-D3BJ/aug-cc-pVTZ optimized electron densities of TNT under an electric field applied along the x-direction viewed along x, y, and z directions. Isosurface values are 0.0004 \|e\|/Å³.

Electric Field (a.u.)	Electric Field (V/m)	View along X-direction	View along Y-direction	View along Z-direction
0	0	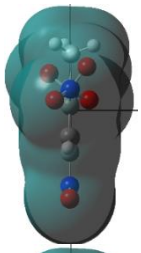	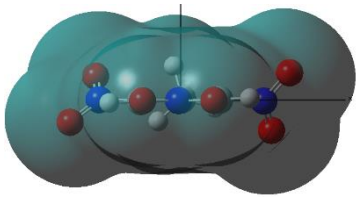	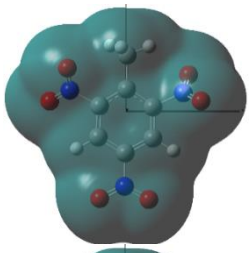
0.0001	5.1×10^7	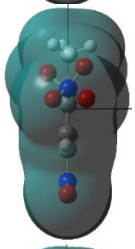	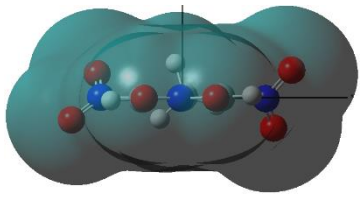	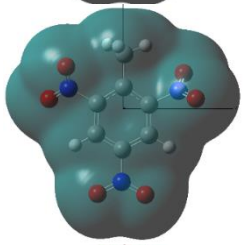
0.0005	2.6×10^8	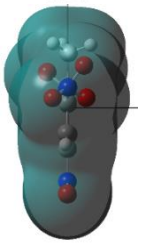	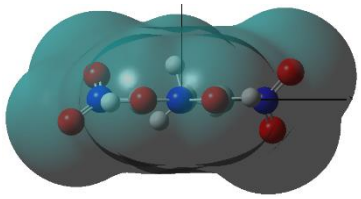	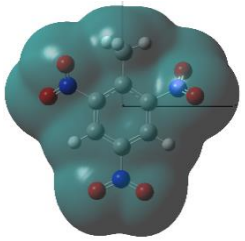
0.001	5.1×10^8	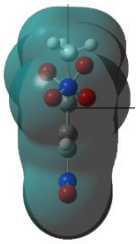	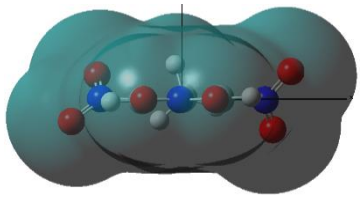	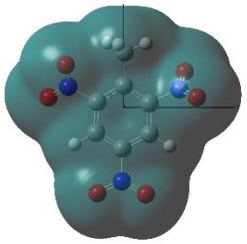
0.005	2.6×10^9	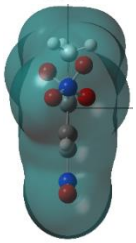	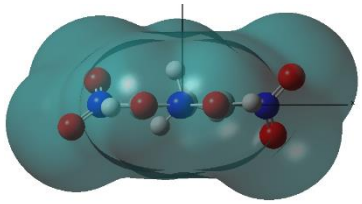	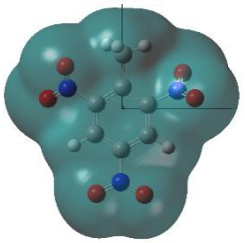
0.01	5.1×10^9	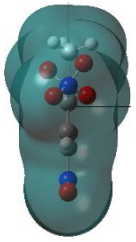	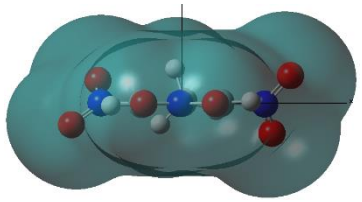	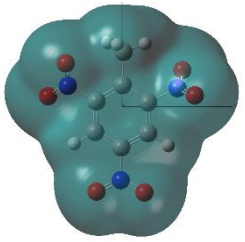

Figure 8. B3LYP-D3BJ/aug-cc-pVTZ optimized electron densities of TNT under an electric field applied along the y-direction viewed along x, y, and z directions. Isosurface values are 0.0004 \|e\|/Å³.

Electric Field (a.u.)	Electric Field (V/m)	View along X-direction	View along Y-direction	View along Z-direction
0	0	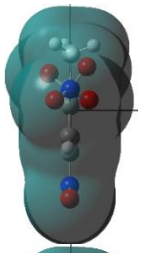	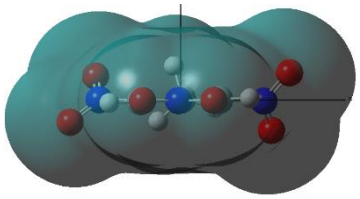	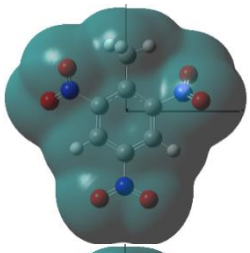
0.0001	5.1×10^{7}	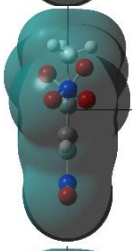	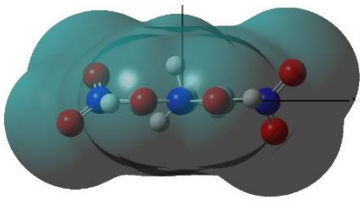	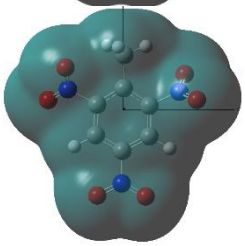
0.0005	2.6×10^{8}	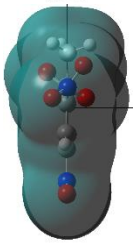	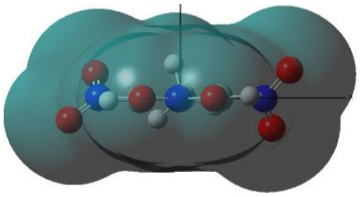	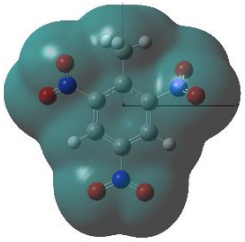
0.001	5.1×10^{8}	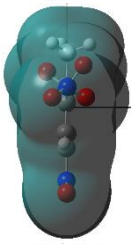	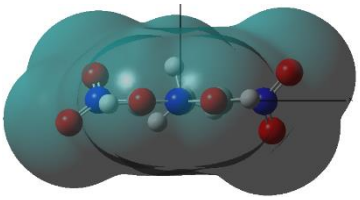	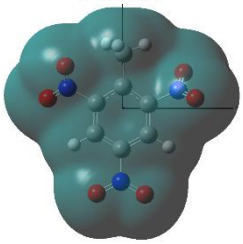
0.005	2.6×10^{9}	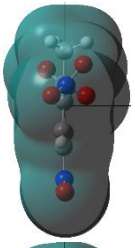	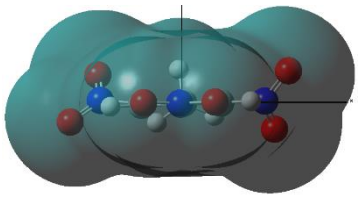	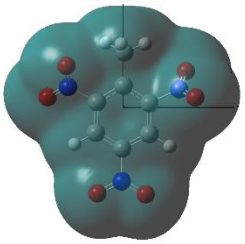
0.01	5.1×10^{9}	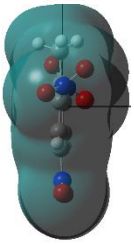	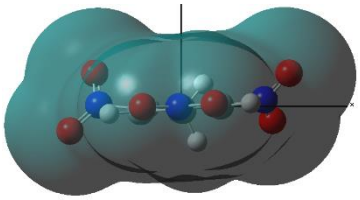	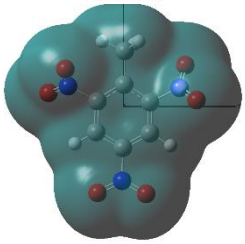

Figure 9. B3LYP-D3BJ/aug-cc-pVTZ optimized electron densities of TNT under an electric field applied along the z-direction viewed along x, y, and z directions. Isosurface values are 0.0004 \|e\|/Å³.

Electric Field (a.u.)	Electric Field (V/m)	View along X-direction	View along Y-direction	View along Z-direction
0	0	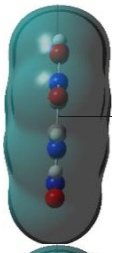	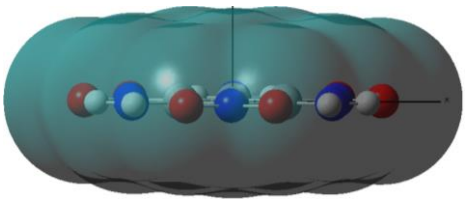	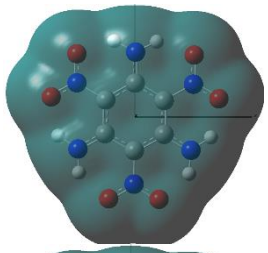
0.0001	5.1×10^{7}	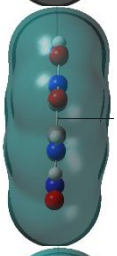	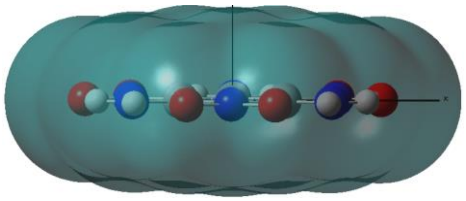	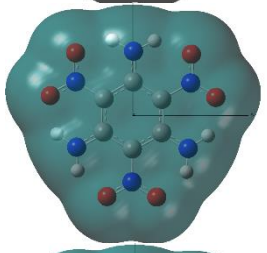
0.0005	2.6×10^{8}	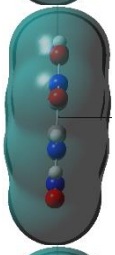	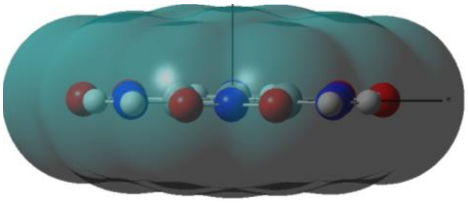	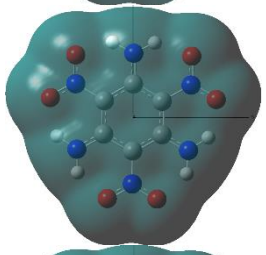
0.001	5.1×10^{8}	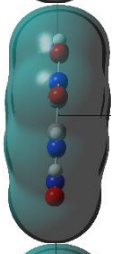	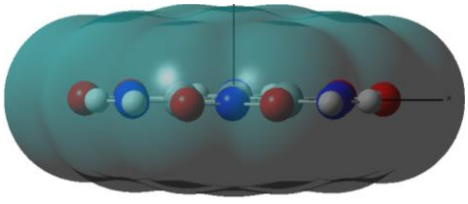	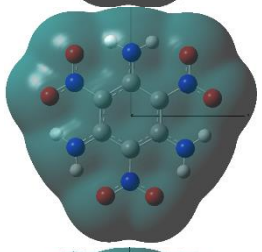
0.005	2.6×10^{9}	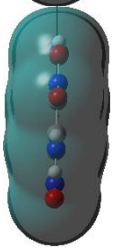	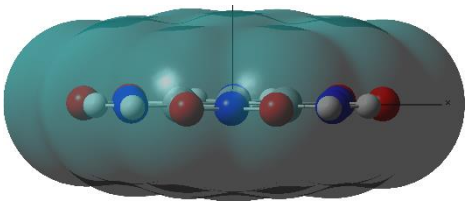	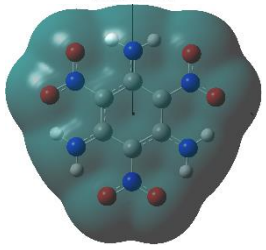

Figure 10. B3LYP-D3BJ/aug-cc-pVDZ optimized electron densities of TATB under an electric field applied along the x-direction viewed along x, y, and z directions. Isosurface values are 0.0004 |e|/Å³.

Electric Field (a.u.)	Electric Field (V/m)	View along X-direction	View along Y-direction	View along Z-direction
0	0	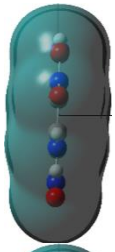	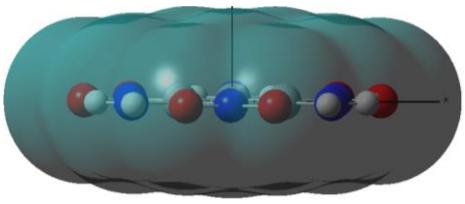	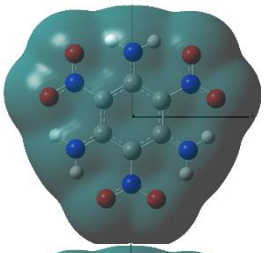
0.0001	5.1×10^{7}	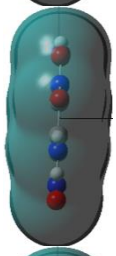	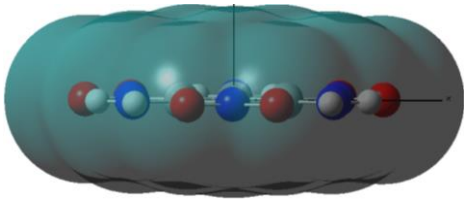	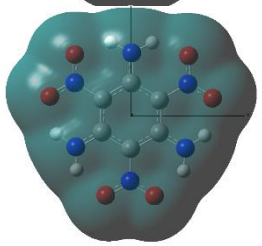
0.0005	2.6×10^{8}	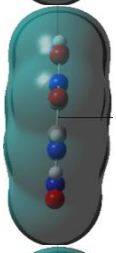	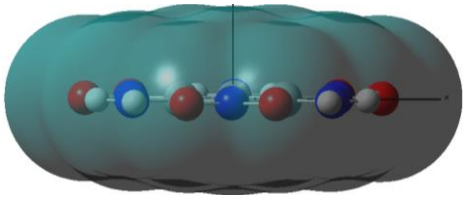	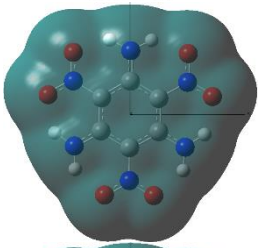
0.001	5.1×10^{8}	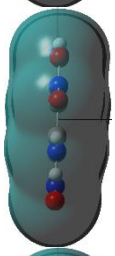	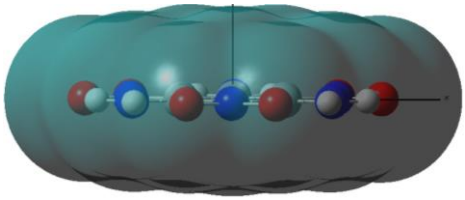	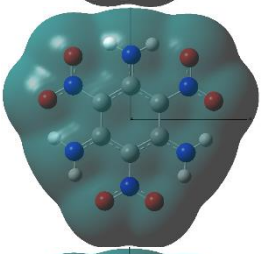
0.005	2.6×10^{9}	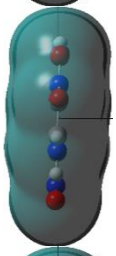	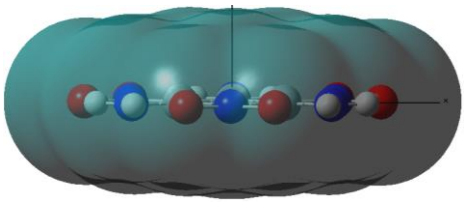	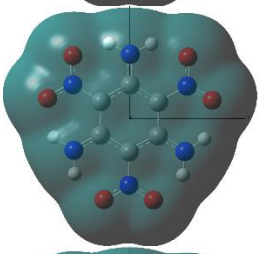
0.01	5.1×10^{9}	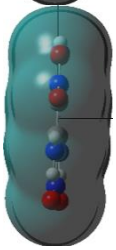	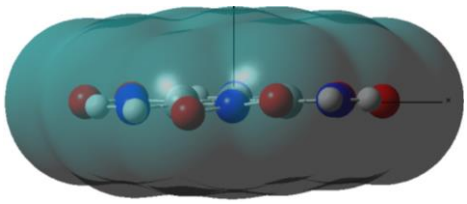	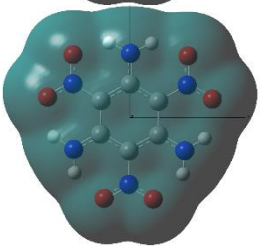

Figure 11. B3LYP-D3BJ/aug-cc-pVDZ optimized electron densities of TATB under an electric field applied along the y-direction viewed along x, y, and z directions. Isosurface values are 0.0004 \|e\|/Å³.

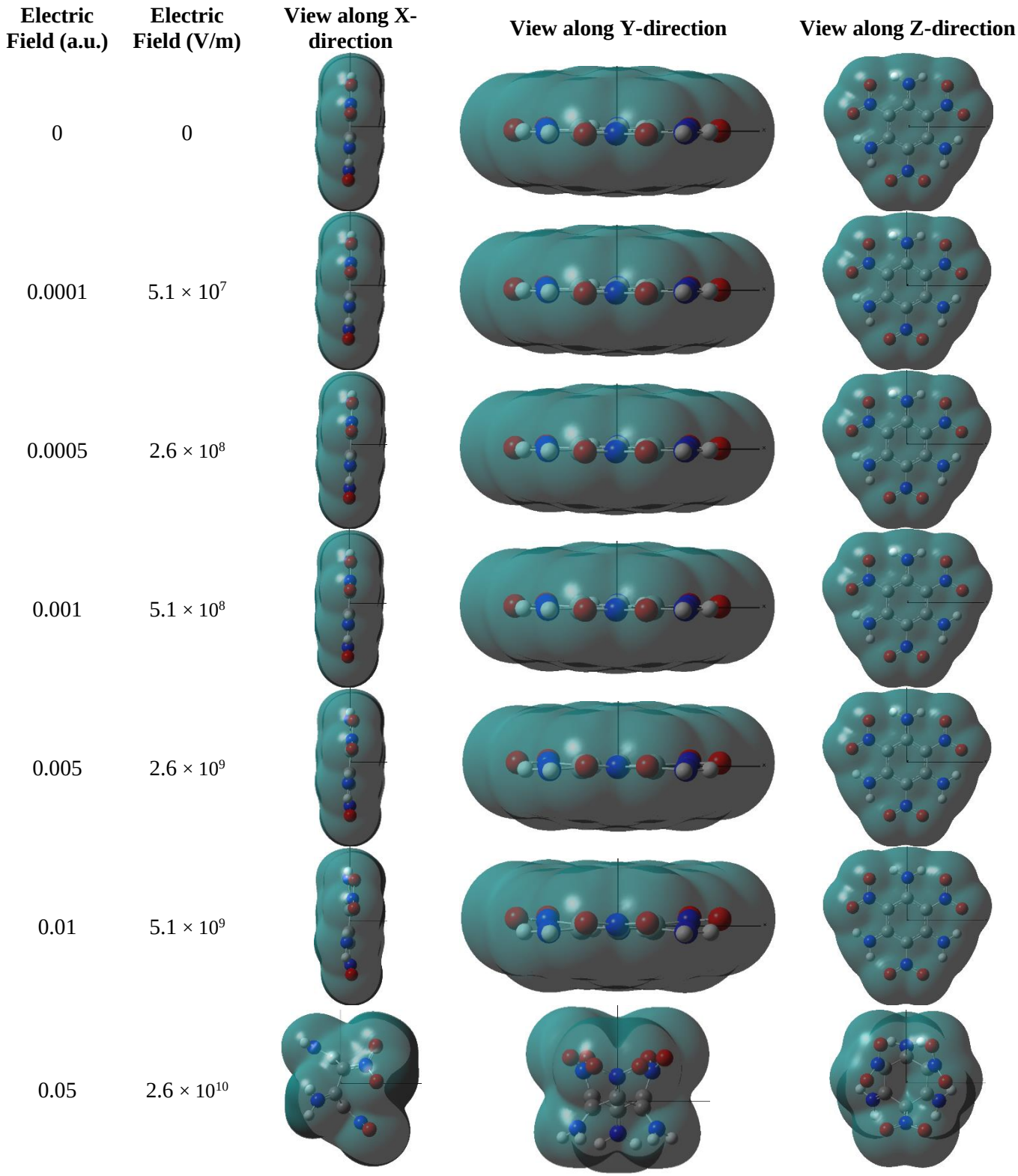

Figure 12. B3LYP-D3BJ/aug-cc-pVDZ optimized electron densities of TATB under an electric field applied along the z-direction viewed along x, y, and z directions. Isosurface values are 0.0004 |e|/Å³.

Electric Field (a.u.)	Electric Field (V/m)	View along X-direction	View along Y-direction	View along Z-direction
0	0	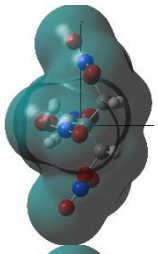	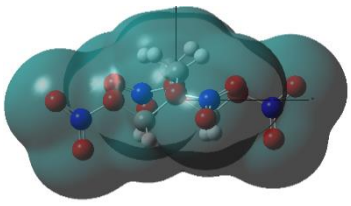	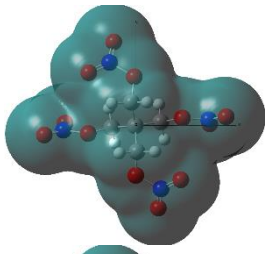
0.0001	5.1×10^{7}	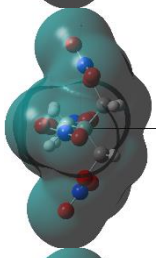	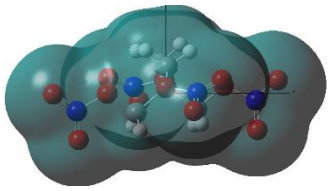	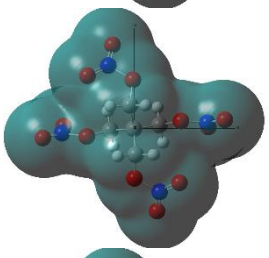
0.0005	2.6×10^{8}	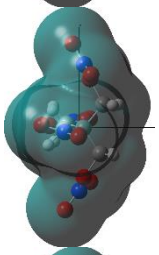	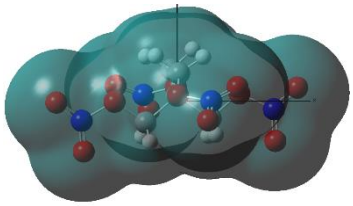	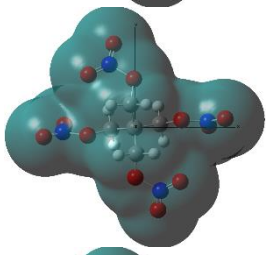
0.001	5.1×10^{8}	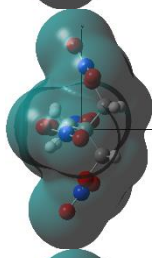	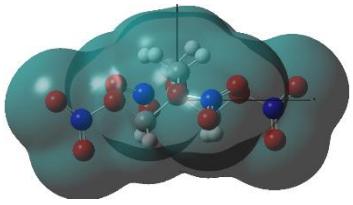	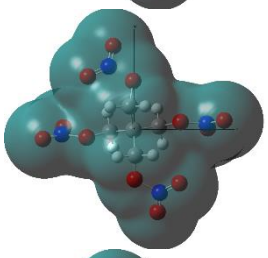
0.005	2.6×10^{9}	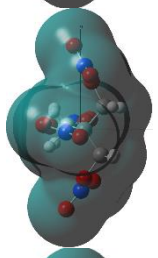	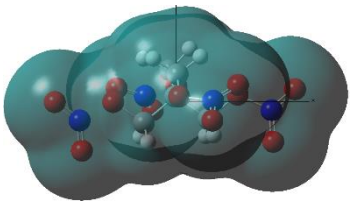	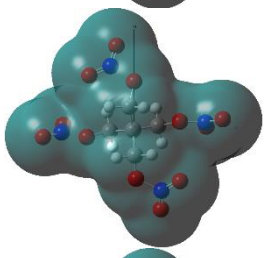
0.01	5.1×10^{9}	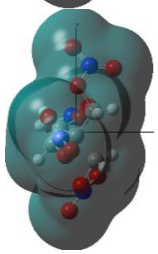	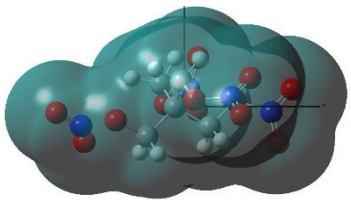	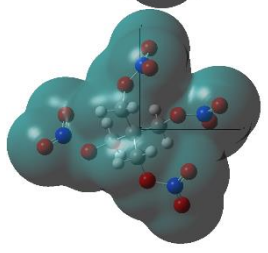

Figure 13. B3LYP-D3BJ/aug-cc-pVTZ optimized electron densities of PETN under an electric field applied along the x-direction viewed along x, y, and z directions. Isosurface values are 0.0004 \|e\|/Å³.

Electric Field (a.u.)	Electric Field (V/m)	View along X-direction	View along Y-direction	View along Z-direction
0	0	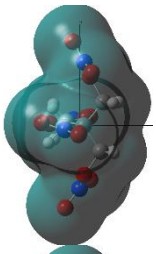	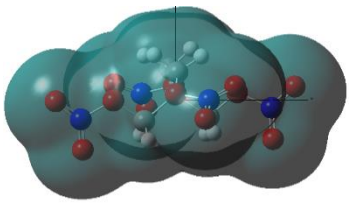	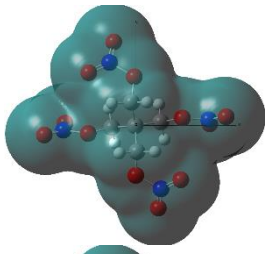
0.0001	5.1×10^{7}	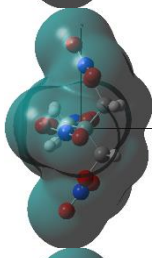	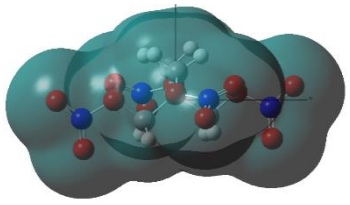	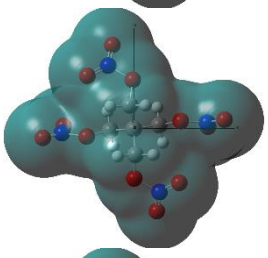
0.0005	2.6×10^{8}	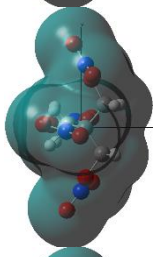	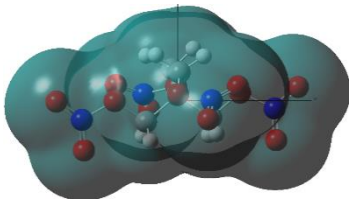	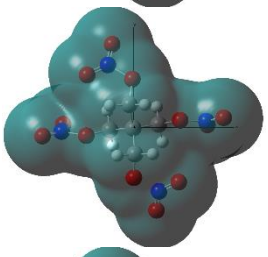
0.001	5.1×10^{8}	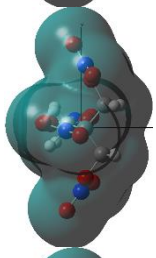	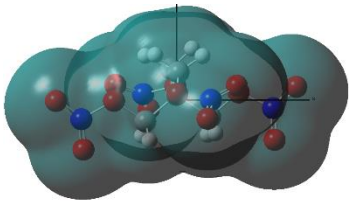	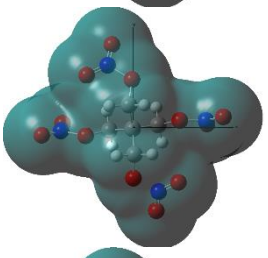
0.005	2.6×10^{9}	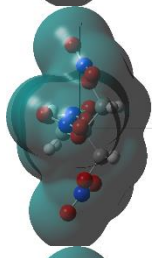	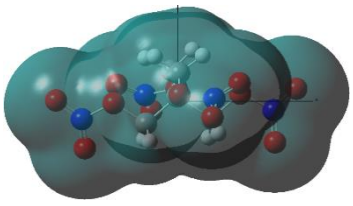	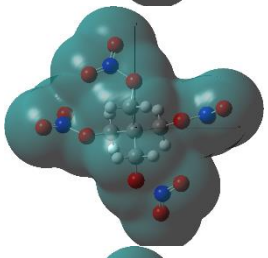
0.01	5.1×10^{9}	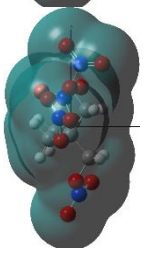	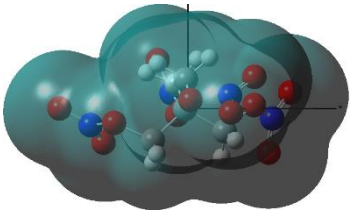	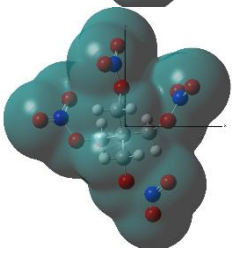

Figure 14. B3LYP-D3BJ/aug-cc-pVTZ optimized electron densities of PETN under an electric field applied along the y-direction viewed along x, y, and z directions. Isosurface values are 0.0004 \|e\|/Å³.

Electric Field (a.u.)	Electric Field (V/m)	View along X-direction	View along Y-direction	View along Z-direction
0	0	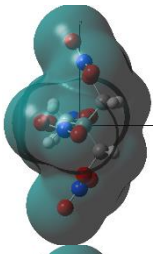	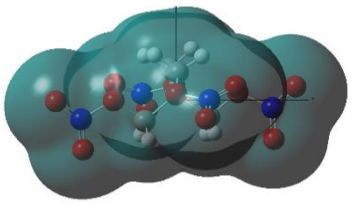	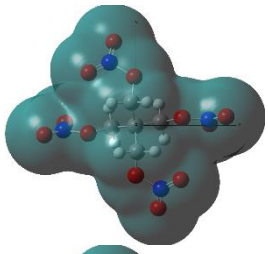
0.0001	5.1×10^{7}	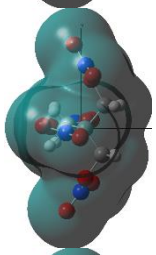	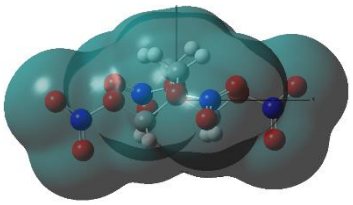	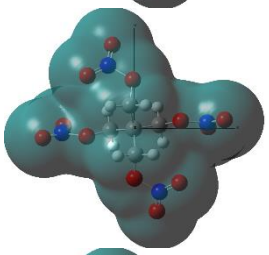
0.0005	2.6×10^{8}	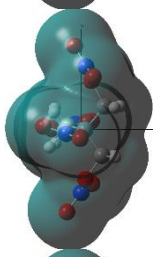	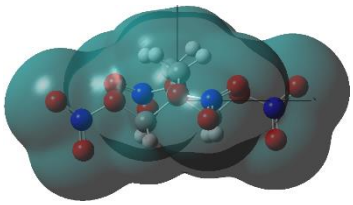	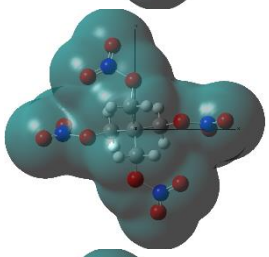
0.001	5.1×10^{8}	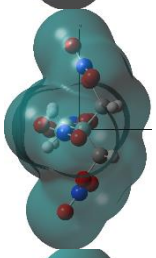	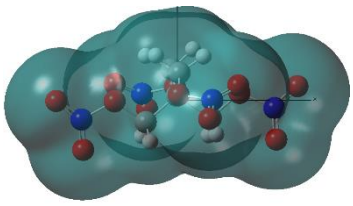	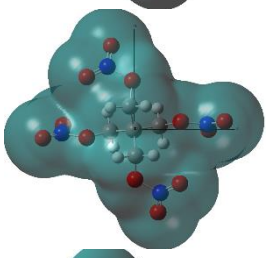
0.005	2.6×10^{9}	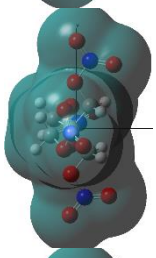	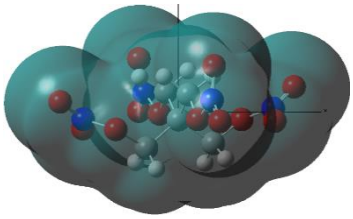	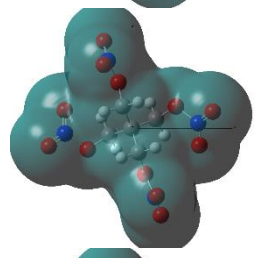
0.01	5.1×10^{9}	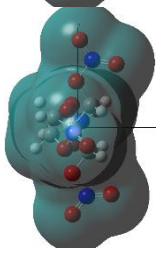	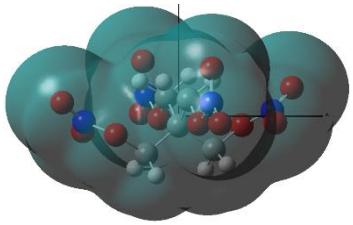	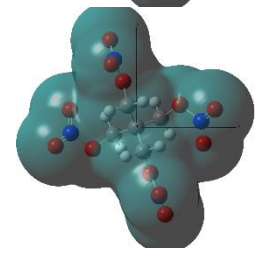

Figure 15. B3LYP-D3BJ/aug-cc-pVTZ optimized electron densities of PETN under an electric field applied along the z-direction viewed along x, y, and z directions. Isosurface values are 0.0004 \|e\|/Å³.

Potential Decomposition Products

One reason for performing calculations with applied electric fields was to determine the effect of the electric field on the decomposition of the HEs, including the activation energy for the first step in the decomposition. In order to do this, potential decomposition products were made computationally to optimize both with and without electric fields to quantify the effect of the field. The optimized decomposition products could then be used as the ending points on transition state searches, with the HEs optimized under electric fields as the starting points. A transition state search could give the actual transition state on the path between these end points and could be used to determine the activation energy of the pathway. After a literature review, the commonly reported pathways for decomposition of these HEs had in common the removal of NO_2 by breaking of the O_2N- bond to either C, N, or O depending on the HE molecular structure [14-17]. Due to the anisotropic nature of applying electric fields along different molecular directions, each nitro group was removed for each HE, yielding 3 (RDX, TNT, TATB) or 4 (PETN) different potential decomposition products to optimize and compare. Figure 16 shows the different nitro groups on the HEs color coordinated with the orientation of the group. The N-R (R = C, N, O) bond lengths were extended to 1.5 Å longer than the previously optimized structures (about the length of the optimized R-N bond length), with a minimum distance of 2.7 Å, to simulate the removal of the NO_2 group from the HE. The 3 decomposition products of RDX were denoted RDX-top, RDX-left, and RDX-right. The 3 decomposition products of TNT were denoted TNT-bottom, TNT-left, and TNT-right. The 3 decomposition products of TATB were denoted TATB-top, TATB-left, and TATB-right. The 4 decomposition products of PETN were denoted PETN-top, PETN-bottom, PETN-left, and PETN-right. These products were first optimized without any electric fields to get a baseline for comparison. Then, the optimized geometries of the decomposition products (without electric fields) were used as the stating guesses for optimizations under the electric fields. The magnitudes and orientations of the electric fields were the same as those used during the optimizations of the initial HE structures.

After optimizing the HE decomposition products, it was found that only the RDX and PETN decomposition products were optimized to a new species with a free nitro group. All of the TNT and TATB decomposition products with lengthened C-NO_2 bonds (2.94 Å) were optimized structures without free nitro groups (the lengthened C-NO_2 bond lengths became ~ 1.4 Å), regardless of the addition of an electric field. These optimized C-NO_2 bonds were shorter than the other C-NO_2 bonds in the same structure (~1.5 Å). This suggests that the initial lengthening of the C-NO_2 bonds at 2.94 Å was not long enough to reduce the interaction and allow the -NO_2 group to leave the rest of the HE structure. Instead, it seemed that the stretched bond rebounded and reached a minimum value around 1.4 Å. Further calculations could be performed to determine the initial C-NO_2 distance which leads to an optimized structure with a free NO_2 group.

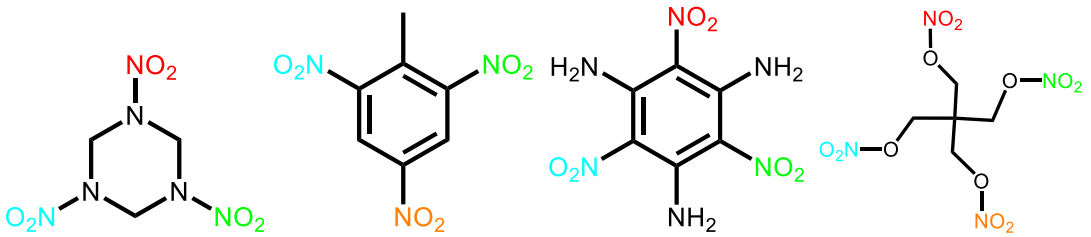

Figure 16. Chemical structures of the HEs in the study with colored nitro groups corresponding to the decomposition products. Red signifies the top nitro group, light blue identifies the left nitro group, light green identifies the right nitro group, and orange signifies the bottom nitro group. The naming convention HE-direction has the nitro group in that direction moved away from the rest of the previously optimized HE structure, in the direction of the bond.

Figures Figure 17 – Figure 19 show how the electron density of the RDX-top species interacted with the applied electric fields oriented along different molecular axes. Similar figures can be found for RDX-left (Figures Figure 20 – Figure 22) and RDX-right (Figures Figure 23 – Figure 25). RDX-top underwent a ring twist under an applied electric field with a magnitude of 2.6×10^9 V/m along the molecular x-direction (Figure 16). This ring twist was accompanied by a change in the direction of the nitro group in the left position, from along the plane of the

molecule to pointing up out of the plane. This led to the change in electron density seen in Figure 17 in the view along the y-direction at this field magnitude. When electric fields were applied at different magnitudes along the molecular y-axis (Figure 18), there were no major changes in the geometries and associated electron densities. The applied electric field along the molecular z-axis at a magnitude of 2.6×10^9 V/m caused the RDX ring to form a bowl-like structure and the free, top nitro group to rotate out of plane (Figure 19). RDX-left also had a ring twist at strong magnitude electric fields along the molecular x-axis, but at a magnitude of 5.1×10^9 V/m, RDX actually optimized with a long C-N distance in the ring, thus breaking the ring in the image produced by the GaussView program (Figure 20). RDX-left underwent small geometrical and electron density changes with applied electric fields along the molecular y-axis, as well as the molecular z-axis (Figures Figure 21 - Figure 22). RDX-right mainly had the free nitro group move along the axis of the applied electric field, with no major changes to the geometry of the remainder of the RDX structure (Figures Figure 23 - Figure 25). Table VI shows the changes in N-NO_2 bond length due to the application of electric fields with varying orientations and magnitudes around the RDX potential decomposition products.

Figures Figure 26 – Figure 28 show the electron density of PETN-top optimized under applied electric fields with different magnitudes applied along different molecular axes. Analogous figures for PETN-bottom (Figures Figure 29 – Figure 31), PETN-left (Figures Figure 32 – Figure 34), and PETN-right (Figures Figure 35 – Figure 37) are also presented. Table VII shows the changes in O-NO_2 bond lengths due to the application of electric fields to the potential PETN decomposition products. When the electric fields were applied along the molecular x-axis (Figure 26), the PETN molecule twisted counter-clockwise starting at a magnitude of 2.6×10^9 V/m. The top nitro group also moved outward, along the x-axis, which was due to the applied electric field along this direction. With electric fields applied along the molecular y-axis (Figure 27), PETN-top had the left and right nitrate ester arms moving upwards towards the molecular y-axis, as if the arms were folding up towards the top nitrate ester arm. With this folding occurring, at a magnitude of 5.1×10^9 V/m the molecule turned counter-clockwise and the top nitro group moved towards the y-axis. PETN-top was fairly stable until the magnitude of the electric field reached 5.1×10^9 V/m along the molecular z-axis (Figure 28). Then, the molecule turned counter-clockwise, the bottom nitro group turned from in plane to almost perpendicular to the plane of the molecule, and the free, top nitro group moved towards larger z values, away from the rest of the molecule.

Applying electric fields with different magnitudes along the molecular x-axis of PETN-bottom did not have much impact on the geometry or electron density, until the magnitude reached 5.1×10^9 V/m (Figure 29). At this magnitude, the entire bottom nitrate ester arm moved towards larger x-values, as if it was curling to align with the x-axis. The left nitro group of this PETN-bottom structure also had a lengthened O-NO_2 bond at 1.46 Å, which was long enough to not show bonding interactions in the GaussView program. Similar to the PETN-top structure, when electric fields were applied along the molecular y-axis, the left and right nitrate ester arms began to curl inward towards the y-axis. At a magnitude of 5.1×10^9 V/m along the y-axis, the PETN molecule rotated counter-clockwise and the top nitro group twisted to be perpendicular from its initial arrangement, seen in the pictures at lower and no magnitude applied electric fields (Figure 30). PETN-bottom was mostly stable to electric fields applied along the molecular z-axis, until the magnitude reached 2.6×10^9 V/m, where the top nitro group turned to be perpendicular from its previous orientation (Figure 31). When the magnitude was 5.1×10^9 V/m along the z-axis, the entire PETN molecule optimized in a position that had the majority of the atoms twisted upward towards larger z values, as if it had been rotated around the molecular x-axis. Also, the oxygen on the bottom nitrate ester arm still attached to the rest of the PETN molecule was rotated about 180° around its own axis.

PETN-left had only limited interaction with the electric fields applied along the molecular x-axis (Figure 32), because there were no major changes in geometry and electron density. However, when the electric fields were applied along the molecular y-axis, PETN-left behaved just like PETN-top and PETN-bottom with the left and right nitrate ester arms folding upwards toward the y-axis (Figure 33). Also, the free, left nitro group moved towards the molecular y-axis. When the electric fields were applied along the molecular z-axis (Figure 34), there was limited interaction, until the magnitude reached 2.6×10^9 V/m, when the bottom nitro group turned almost perpendicular from its previous position and the entire molecule turned counter-clockwise.

PETN-right with applied electric fields along the molecular x-axis had the free, right nitro group moving along the x-axis, with the rest of the structure staying relatively constant (Figure 35). PETN-right was different than the other PETN decomposition products in that the left and right arms didn't begin to curl up towards the y-axis until the electric field magnitude reached 5.1×10^9 V/m (Figure 36). The bottom nitro group also did not show a bond in the GaussView program due to a O-NO_2 distance of 1.46 Å. When the electric field was applied along the molecular z-axis, PETN-right remained stable until the magnitude was 2.6×10^9 V/m, when the top nitro group twisted perpendicular to its initial position and the entire molecule turned counter-clockwise (Figure 37).

Table VI. Initial and Final N-NO_2 Bond Lengths in the RDX Structures Optimized With and Without Applied Electric Fields. All Units are Å.

Electric Field	RDX-top		RDX-left		RDX-right	
	Initial	Final	Initial	Final	Initial	Final
0 V/m	2.800	2.320	2.800	2.211	2.800	2.211
5.1×10^7 V/m along x-axis	2.320	2.320	2.211	2.210	2.211	2.211
2.6×10^8 V/m along x-axis	2.320	2.319	2.211	2.210	2.211	2.217
5.1×10^8 V/m along x-axis	2.320	2.318	2.211	2.211	2.211	2.249
2.6×10^9 V/m along x-axis	2.320	2.334	2.211	2.264	2.211	2.491
5.1×10^9 V/m along x-axis	2.320	2.379	2.211	2.287	NA	NA
5.1×10^7 V/m along y-axis	2.320	2.321	2.211	2.211	2.211	2.211
2.6×10^8 V/m along y-axis	2.320	2.326	2.211	2.215	2.211	2.216
5.1×10^8 V/m along y-axis	2.320	2.407	2.211	2.224	2.211	2.225
2.6×10^9 V/m along y-axis	2.320	2.585	2.211	2.343	2.211	2.364
5.1×10^9 V/m along y-axis	NA	NA	2.211	2.611	2.211	2.675
5.1×10^7 V/m along z-axis	2.320	2.322	2.211	2.209	2.211	2.212
2.6×10^8 V/m along z-axis	2.320	2.327	2.211	2.206	2.211	2.217
5.1×10^8 V/m along z-axis	2.320	2.334	2.211	2.204	2.211	2.225
2.6×10^9 V/m along z-axis	2.320	2.575	2.211	2.211	2.211	2.331
5.1×10^9 V/m along z-axis	NA	NA	2.211	2.213	NA	NA

Table VII. Initial and Final O-NO_2 Bond Lengths in the PETN Structures Optimized With and Without Applied Electric Fields. All Units are Å.

Electric Field	PETN-top		PETN-bottom		PETN-left		PETN-right	
	Initial	Final	Initial	Final	Initial	Final	Initial	Final
0 V/m	2.720	2.208	2.720	2.208	2.720	2.207	2.720	2.207
5.1×10^7 V/m along x-axis	2.208	2.208	2.208	2.208	2.207	2.207	2.207	2.206
2.6×10^8 V/m along x-axis	2.208	2.208	2.208	2.208	2.207	2.210	2.207	2.204
5.1×10^8 V/m along x-axis	2.208	2.209	2.208	2.209	2.207	2.213	2.207	2.203
2.6×10^9 V/m along x-axis	2.208	2.232	2.208	2.249	2.207	2.255	2.207	2.209
5.1×10^9 V/m along x-axis	2.208	2.273	2.208	2.441	2.207	2.392	2.207	2.484
5.1×10^7 V/m along y-axis	2.208	2.207	2.208	2.208	2.207	2.207	2.207	2.207
2.6×10^8 V/m along y-axis	2.208	2.205	2.208	2.211	2.207	2.208	2.207	2.206
5.1×10^8 V/m along y-axis	2.208	2.203	2.208	2.214	2.207	2.210	2.207	2.205
2.6×10^9 V/m along y-axis	2.208	2.192	2.208	2.244	2.207	2.242	2.207	2.196
5.1×10^9 V/m along y-axis	2.208	2.402	2.208	2.275	2.207	2.399	2.207	2.414
5.1×10^7 V/m along z-axis	2.208	2.208	2.208	2.208	2.207	2.207	2.207	2.207
2.6×10^8 V/m along z-axis	2.208	2.207	2.208	2.207	2.207	2.208	2.207	2.207
5.1×10^8 V/m along z-axis	2.208	2.206	2.208	2.207	2.207	2.208	2.207	2.208
2.6×10^9 V/m along z-axis	2.208	2.203	2.208	2.206	2.207	2.217	2.207	2.213
5.1×10^9 V/m along z-axis	NA	NA	2.208	2.493	NA	NA	NA	NA

Electric Field (a.u.)	Electric Field (V/m)	View along X-direction	View along Y-direction	View along Z-direction
0	0	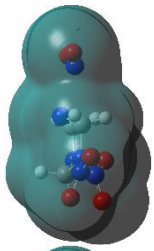	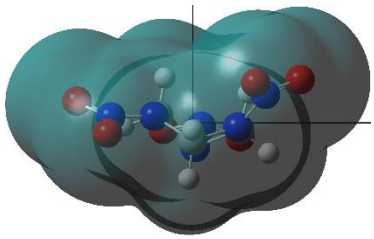	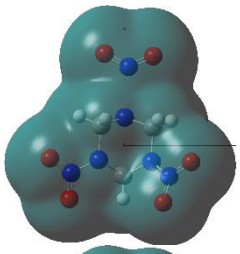
0.0001	5.1×10^7	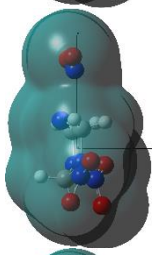	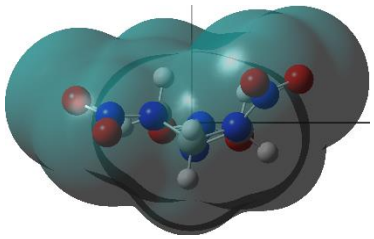	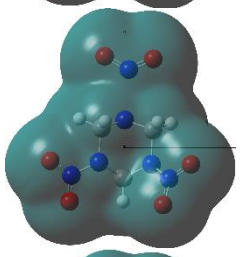
0.0005	2.6×10^8	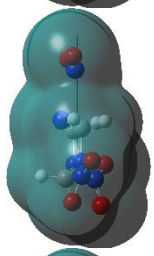	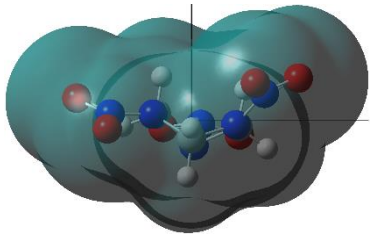	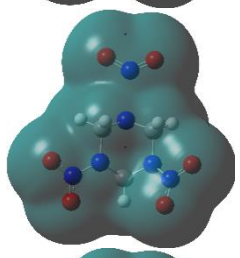
0.001	5.1×10^8	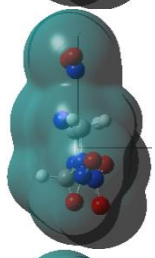	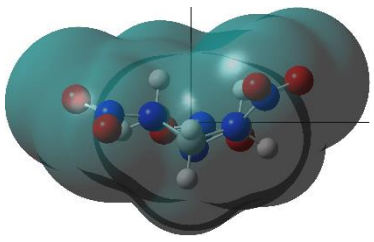	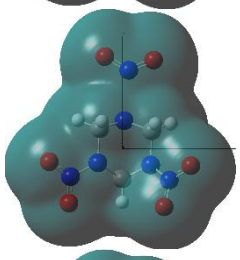
0.005	2.6×10^9	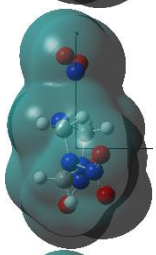	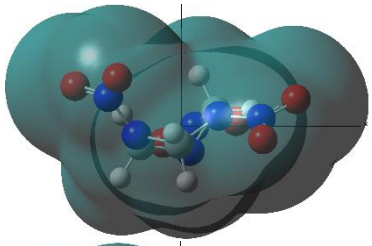	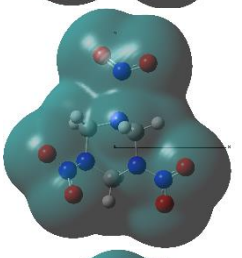
0.01	5.1×10^9	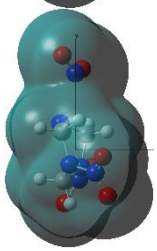	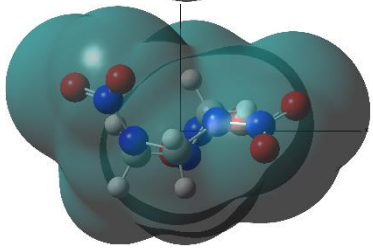	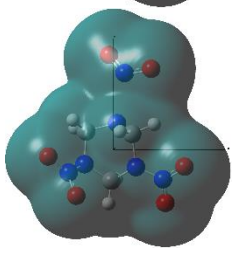

Figure 17. B3LYP-D3BJ/aug-cc-pVTZ optimized electron densities of RDX-top under an electric field applied along the x-direction viewed along x, y, and z directions. Isosurface values are 0.0004 \|e\|/Å^3.

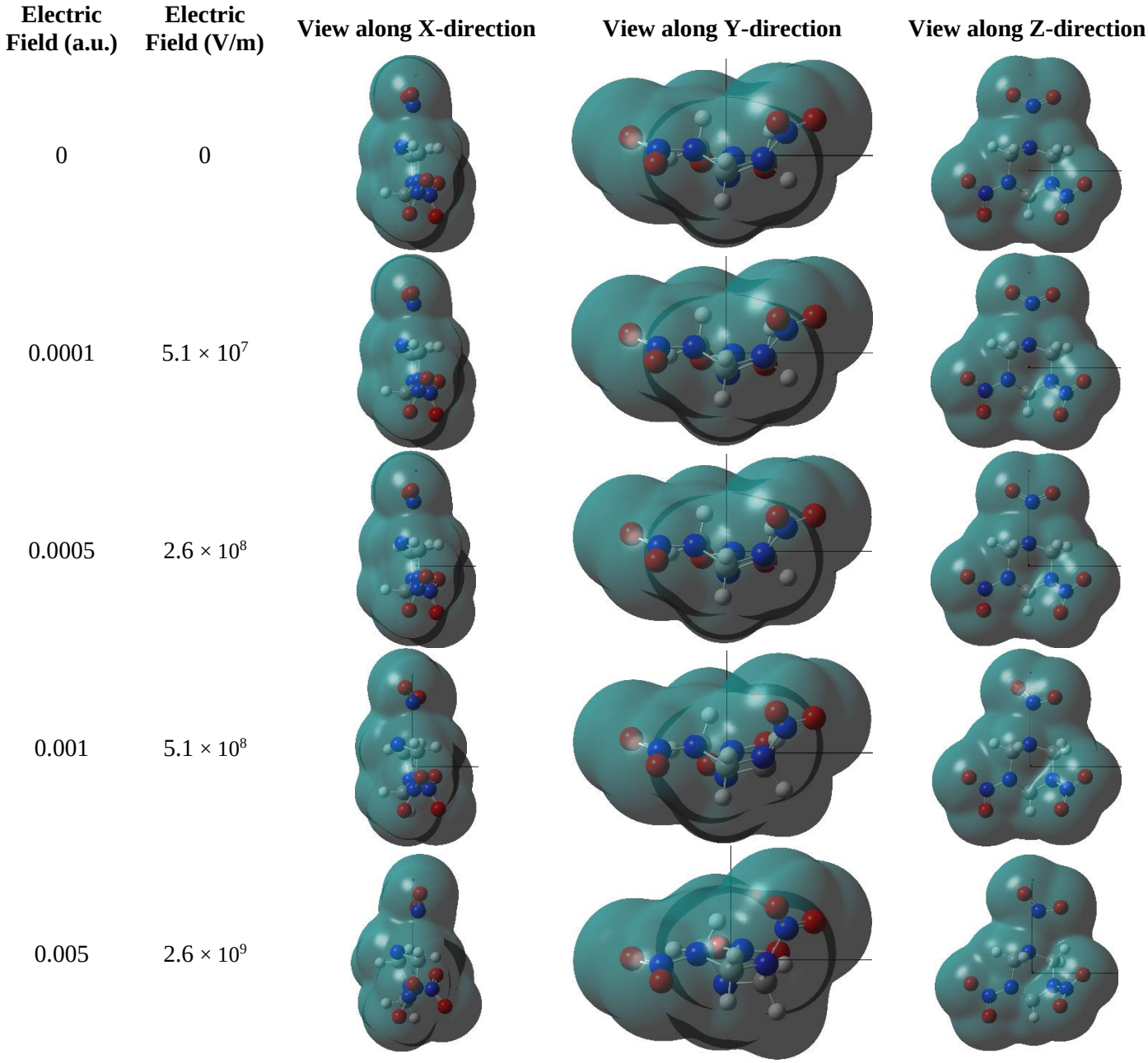

Figure 18. B3LYP-D3BJ/aug-cc-pVTZ optimized electron densities of RDX-top under an electric field applied along the y-direction viewed along x, y, and z directions. Isosurface values are 0.0004 |e|/Å³.

Electric Field (a.u.)	Electric Field (V/m)	View along X-direction	View along Y-direction	View along Z-direction
0	0	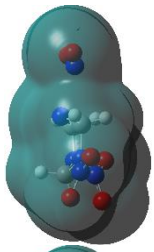	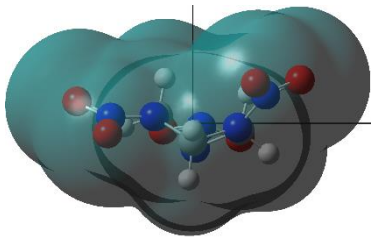	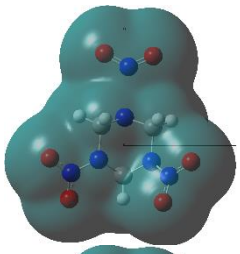
0.0001	5.1×10^7	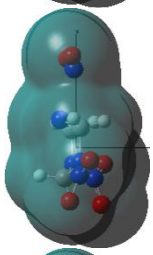	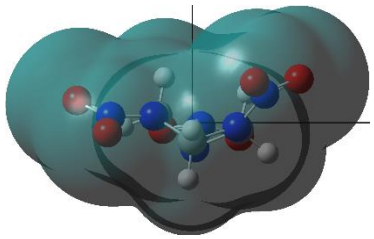	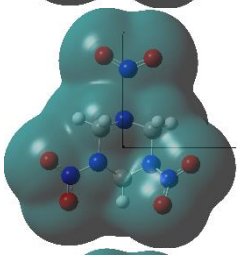
0.0005	2.6×10^8	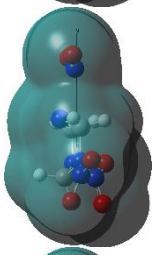	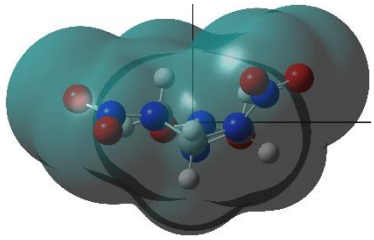	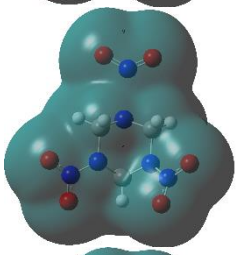
0.001	5.1×10^8	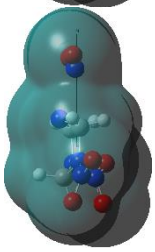	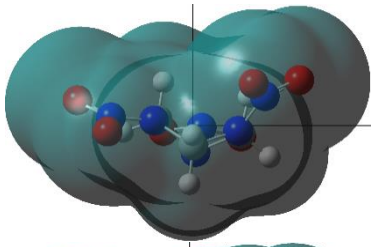	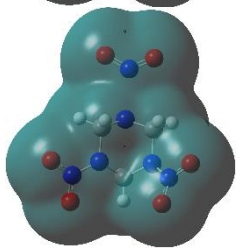
0.005	2.6×10^9	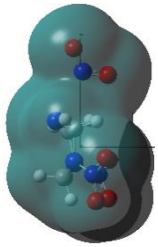	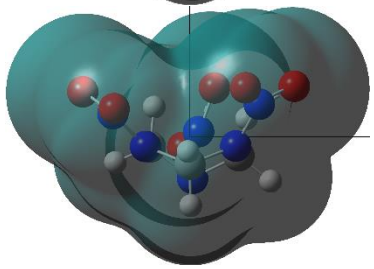	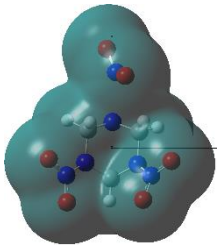

Figure 19. B3LYP-D3BJ/aug-cc-pVTZ optimized electron densities of RDX-top under an electric field applied along the z-direction viewed along x, y, and z directions. Isosurface values are 0.0004 |e|/Å³.

Electric Field (a.u.)	Electric Field (V/m)	View along X-direction	View along Y-direction	View along Z-direction
0	0			
0.0001	5.1×10^7			
0.0005	2.6×10^8			
0.001	5.1×10^8			
0.005	2.6×10^9			
0.01	5.1×10^9			

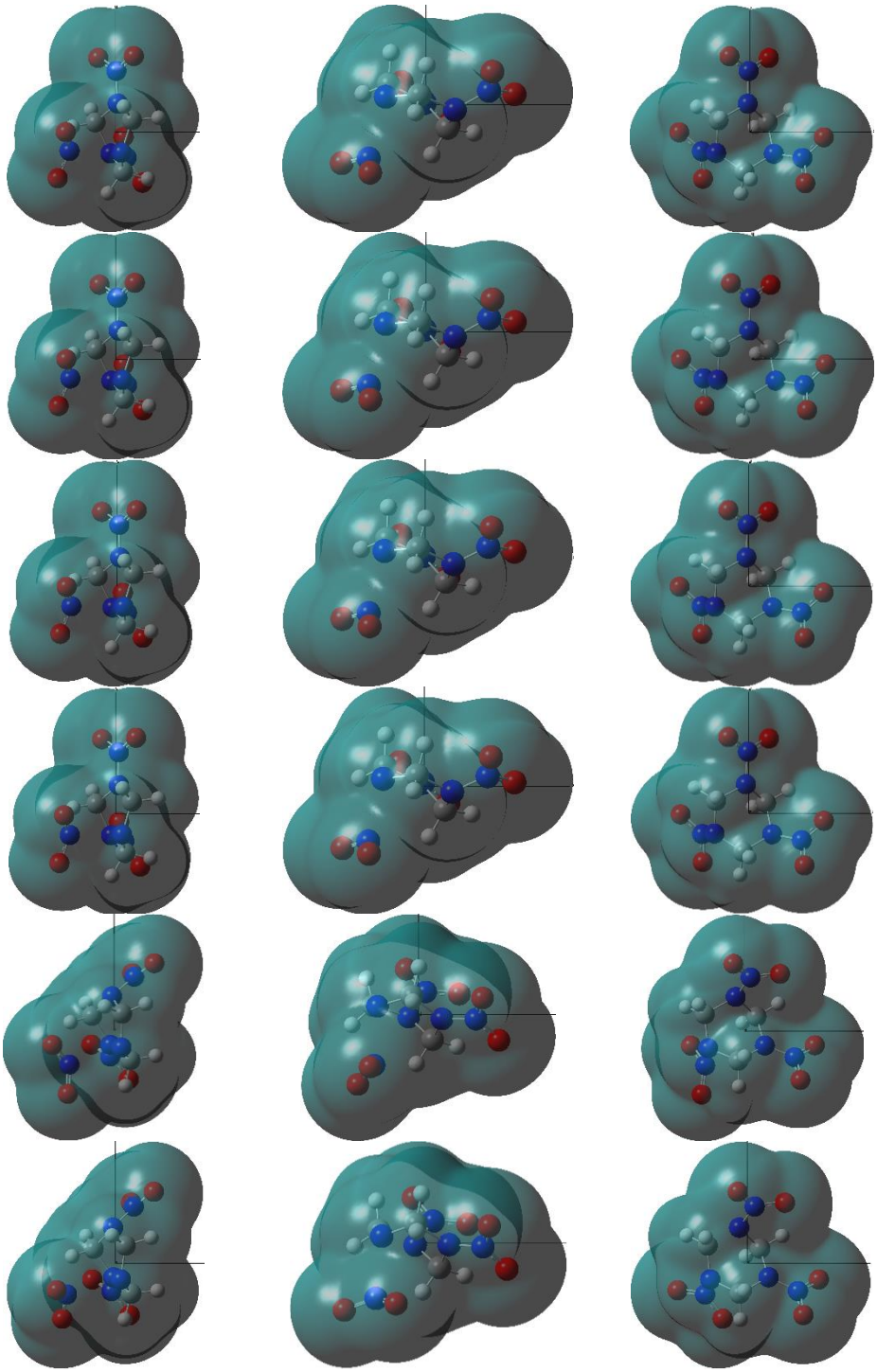

Figure 20. B3LYP-D3BJ/aug-cc-pVTZ optimized electron densities of RDX-left under an electric field applied along the x-direction viewed along x, y, and z directions. Isosurface values are 0.0004 |e|/Å³.

Electric Field (a.u.)	Electric Field (V/m)	View along X-direction	View along Y-direction	View along Z-direction
0	0	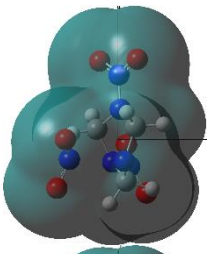	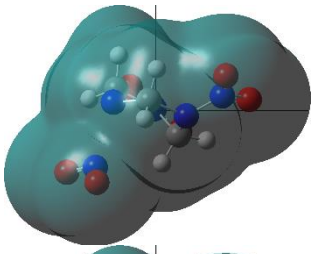	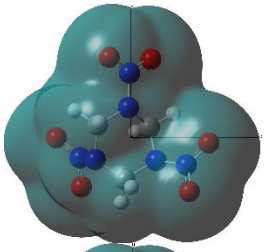
0.0001	5.1×10^7	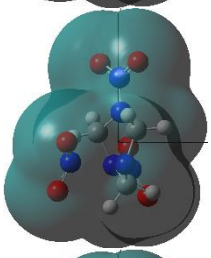	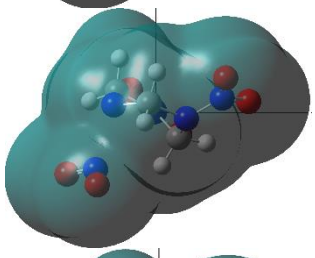	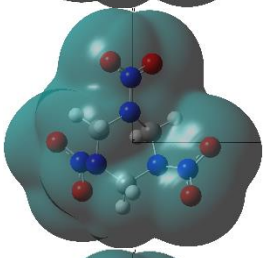
0.0005	2.6×10^8	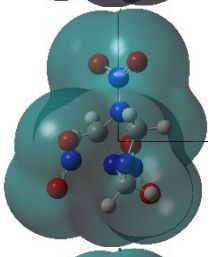	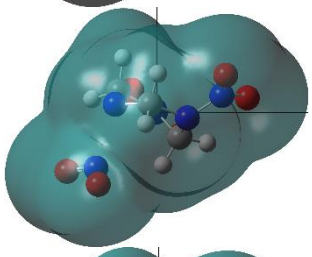	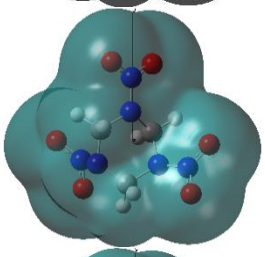
0.001	5.1×10^8	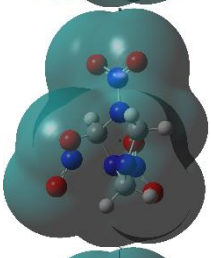	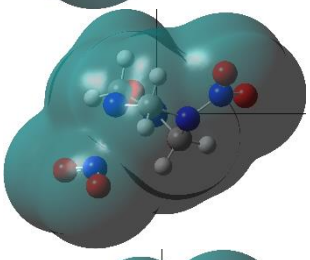	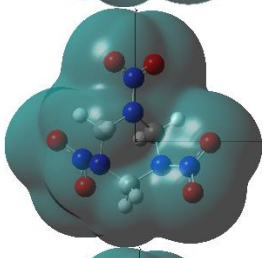
0.005	2.6×10^9	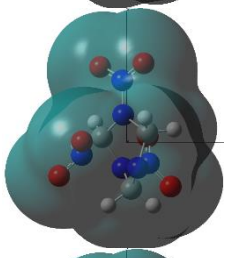	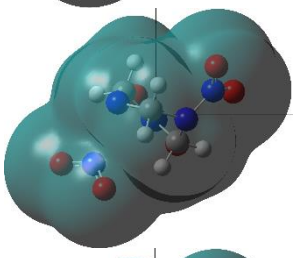	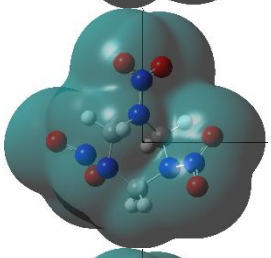
0.01	5.1×10^9	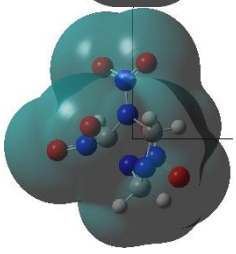	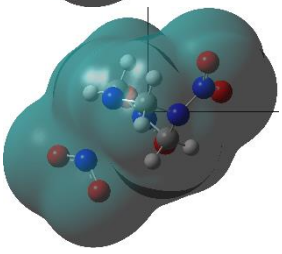	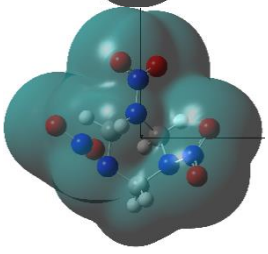

Figure 21. B3LYP-D3BJ/aug-cc-pVTZ optimized electron densities of RDX-left under an electric field applied along the y-direction viewed along x, y, and z directions. Isosurface values are 0.0004 |e|/Å³.

Electric Field (a.u.)	Electric Field (V/m)	View along X-direction	View along Y-direction	View along Z-direction
0	0	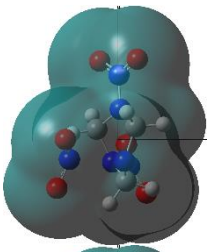	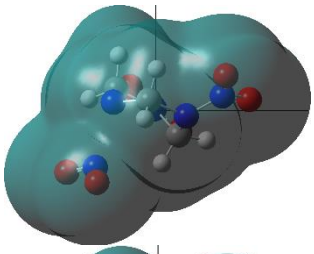	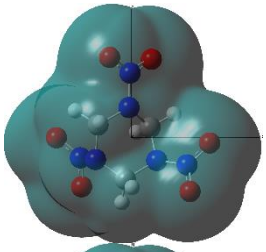
0.0001	5.1×10^7	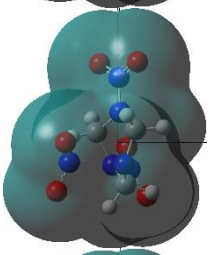	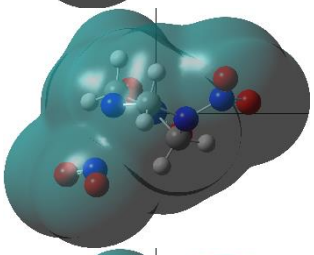	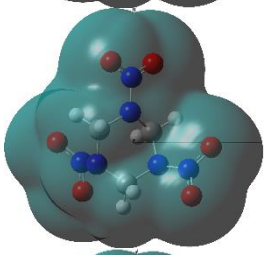
0.0005	2.6×10^8	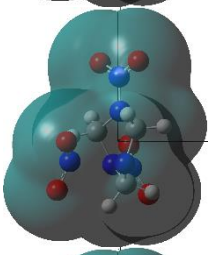	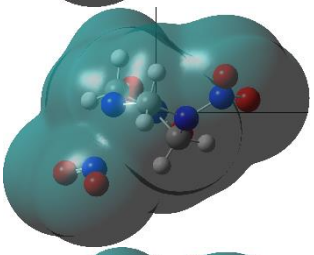	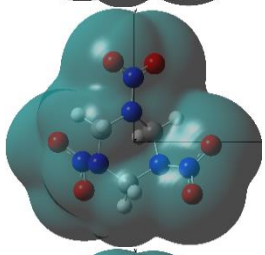
0.001	5.1×10^8	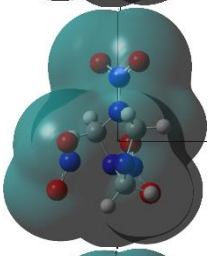	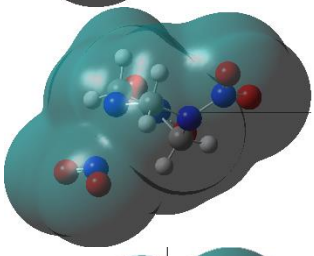	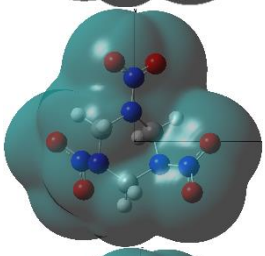
0.005	2.6×10^9	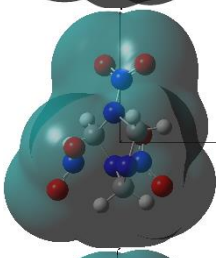	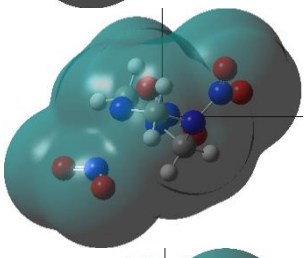	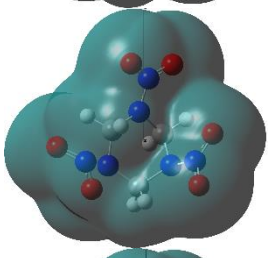
0.01	5.1×10^9	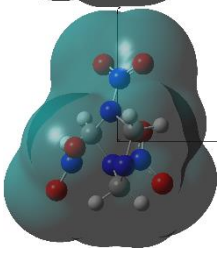	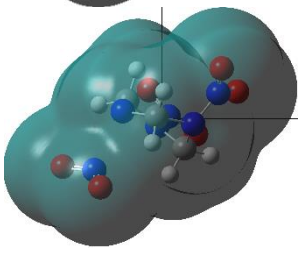	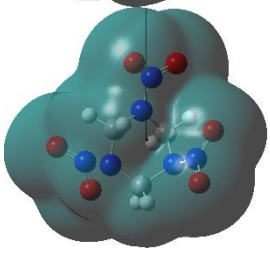

Figure 22. B3LYP-D3BJ/aug-cc-pVTZ optimized electron densities of RDX-left under an electric field applied along the z-direction viewed along x, y, and z directions. Isosurface values are 0.0004 |e|/Å³.

Electric Field (a.u.)	Electric Field (V/m)	View along X-direction	View along Y-direction	View along Z-direction
0	0	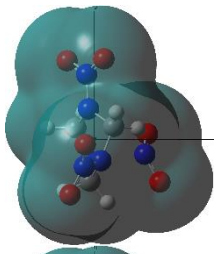	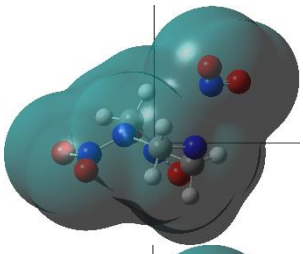	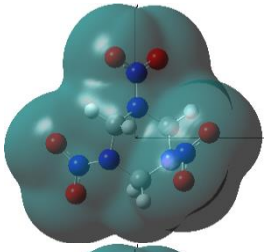
0.0001	5.1×10^7	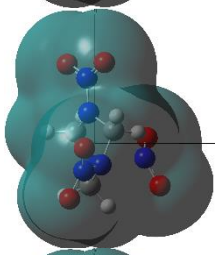	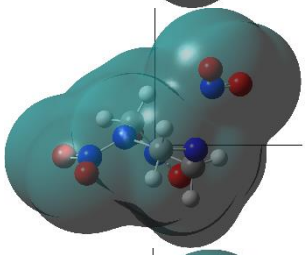	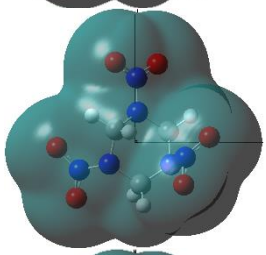
0.0005	2.6×10^8	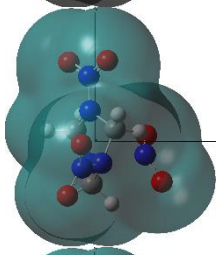	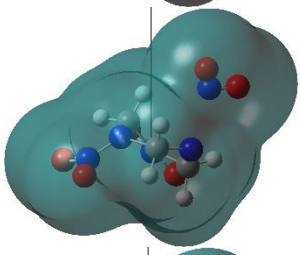	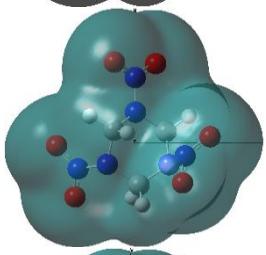
0.001	5.1×10^8	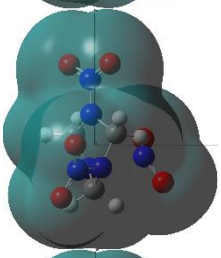	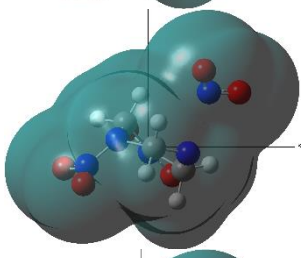	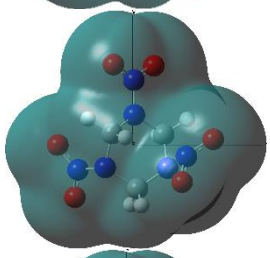
0.005	2.6×10^9	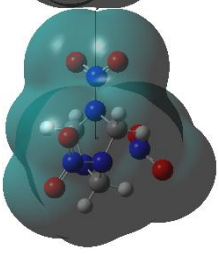	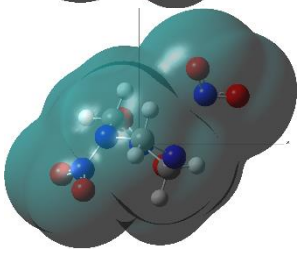	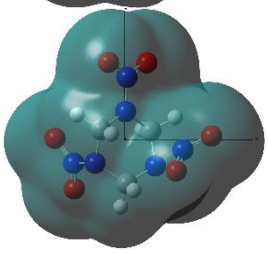

Figure 23. B3LYP-D3BJ/aug-cc-pVTZ optimized electron densities of RDX-right viewed along x, y, and z directions under and electric field applied along the x-direction. Isosurface values are 0.0004 $|e|/Å^3$.

Electric Field (a.u.)	Electric Field (V/m)	View along X-direction	View along Y-direction	View along Z-direction
0	0	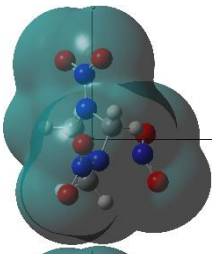	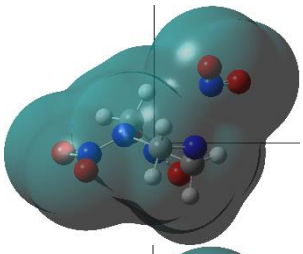	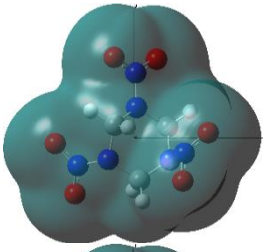
0.0001	5.1×10^7	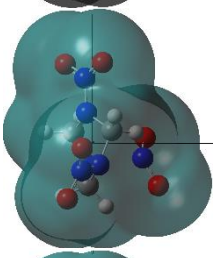	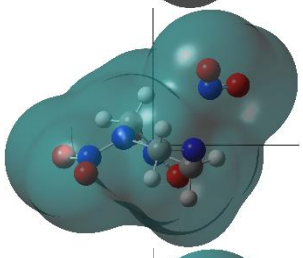	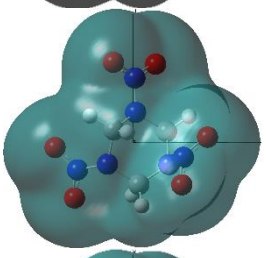
0.0005	2.6×10^8	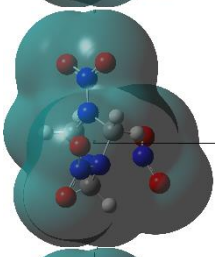	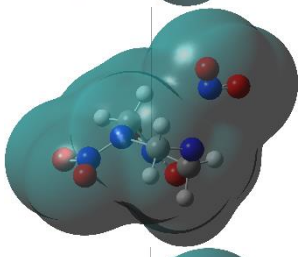	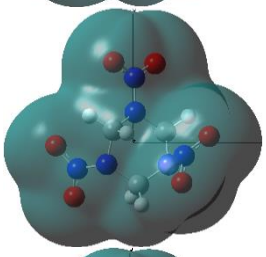
0.001	5.1×10^8	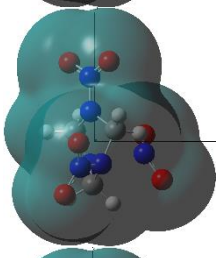	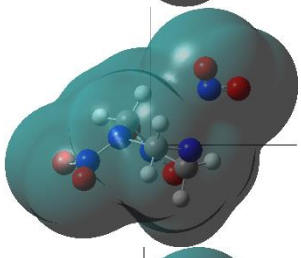	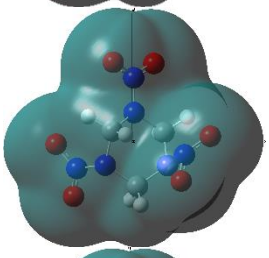
0.005	2.6×10^9	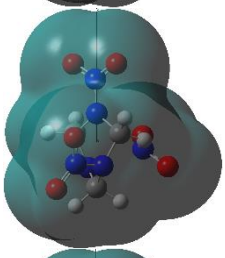	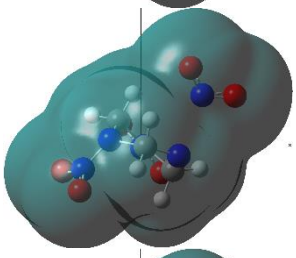	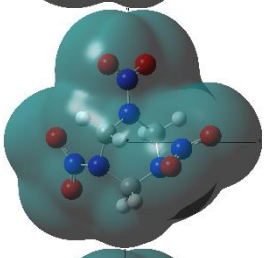
0.01	5.1×10^9	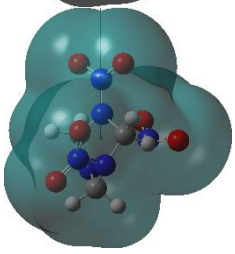	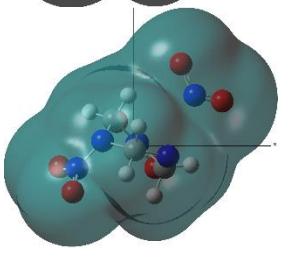	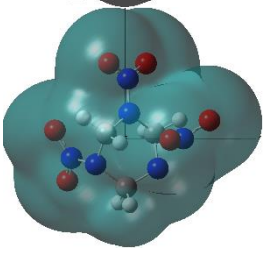

Figure 24. B3LYP-D3BJ/aug-cc-pVTZ optimized electron densities of RDX-right viewed along x, y, and z directions under and electric field applied along the y-direction. Isosurface values are 0.0004 \|e\|/Å³.

Electric Field (a.u.)	Electric Field (V/m)	View along X-direction	View along Y-direction	View along Z-direction
0	0	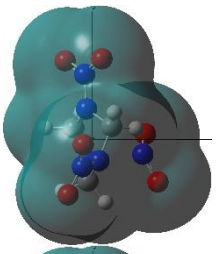	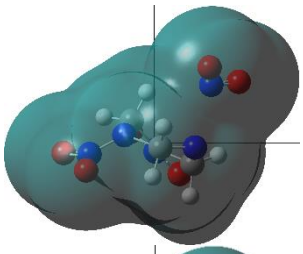	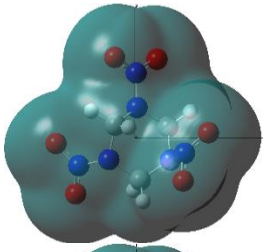
0.0001	5.1×10^7	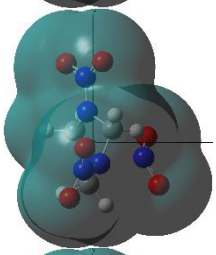	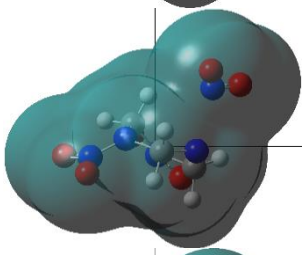	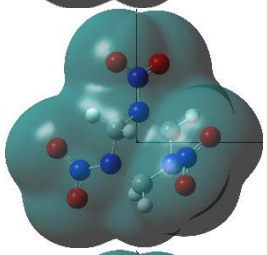
0.0005	2.6×10^8	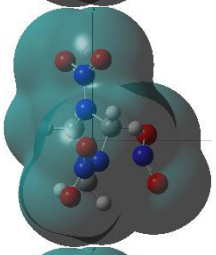	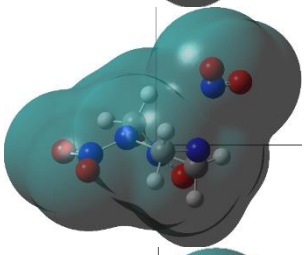	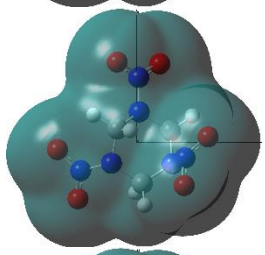
0.001	5.1×10^8	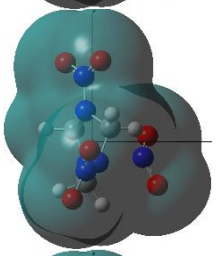	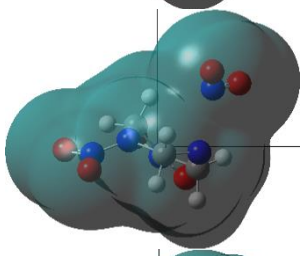	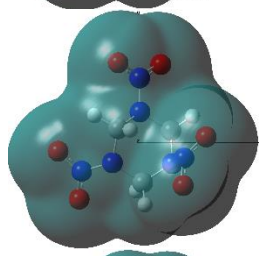
0.005	2.6×10^9	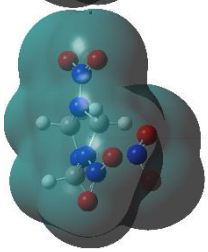	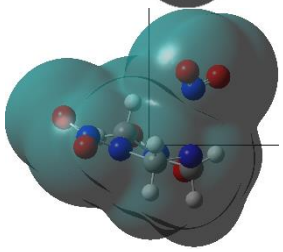	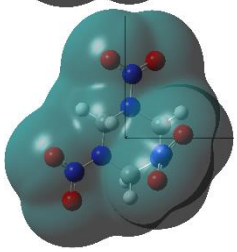

Figure 25. B3LYP-D3BJ/aug-cc-pVTZ optimized electron densities of RDX-right viewed along x, y, and z directions under and electric field applied along the z-direction. Isosurface values are 0.0004 \|e\|/Å³.

Electric Field (a.u.)	Electric Field (V/m)	View along X-direction	View along Y-direction	View along Z-direction
0	0	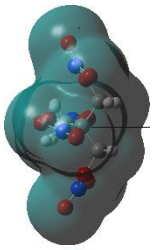	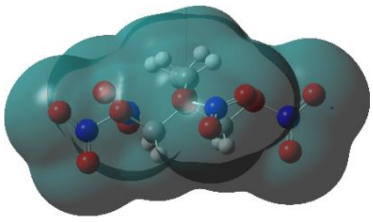	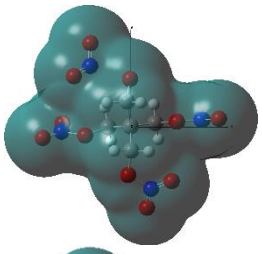
0.0001	5.1×10^7	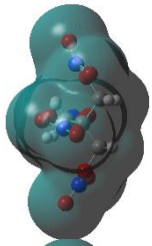	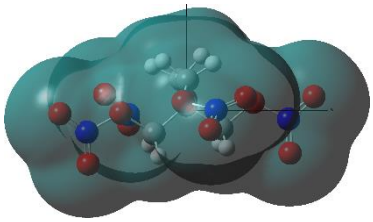	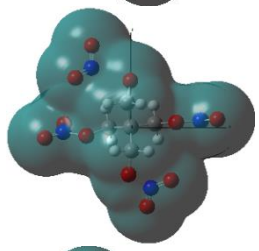
0.0005	2.6×10^8	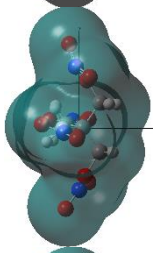	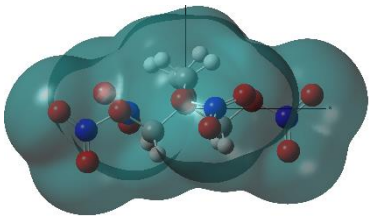	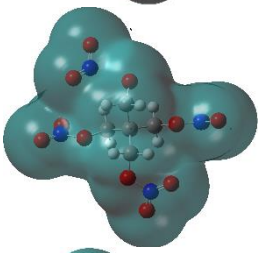
0.001	5.1×10^8	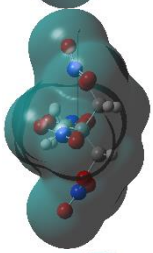	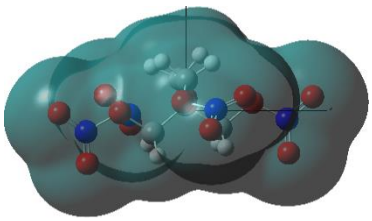	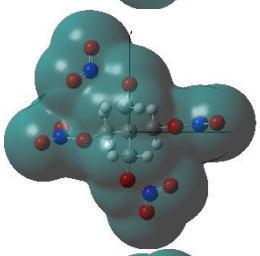
0.005	2.6×10^9	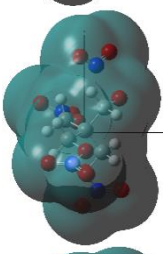	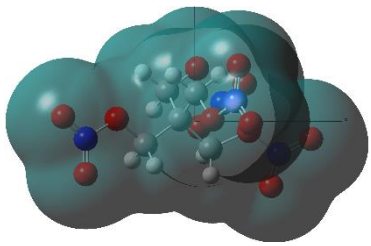	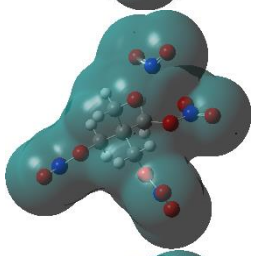
0.01	5.1×10^9	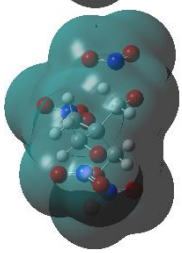	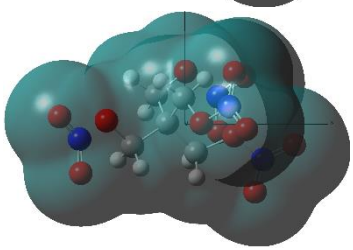	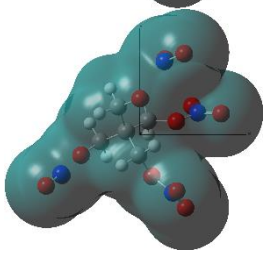

Figure 26. B3LYP-D3BJ/aug-cc-pVTZ optimized electron densities of PETN-top under an electric field applied along the x-direction viewed along x, y, and z directions. Isosurface values are 0.0004 |e|/Å³.

Electric Field (a.u.)	Electric Field (V/m)	View along X-direction	View along Y-direction	View along Z-direction
0	0	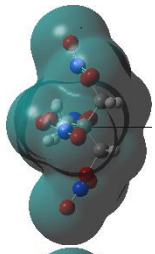	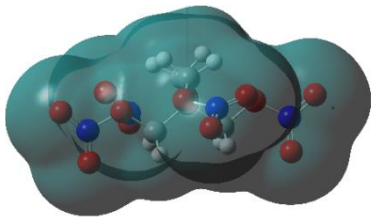	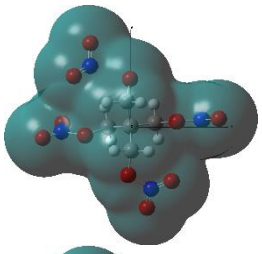
0.0001	5.1×10^7	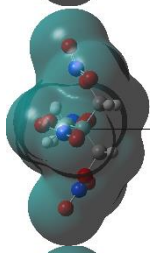	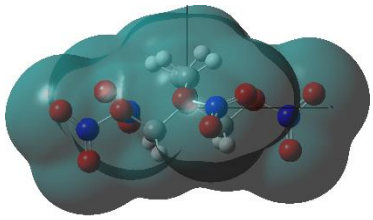	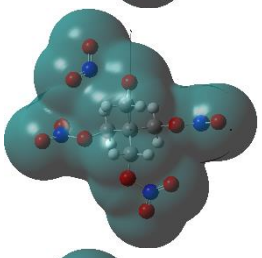
0.0005	2.6×10^8	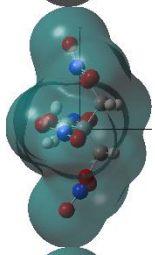	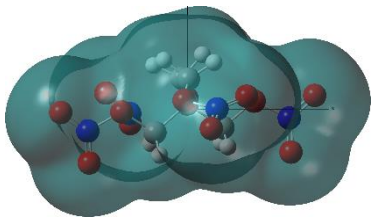	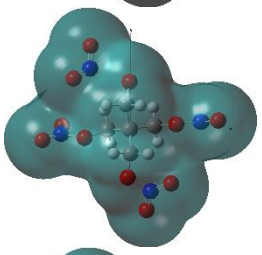
0.001	5.1×10^8	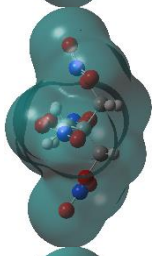	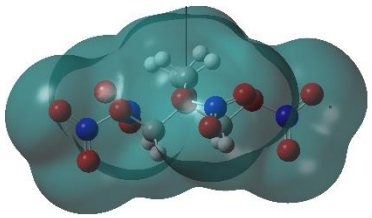	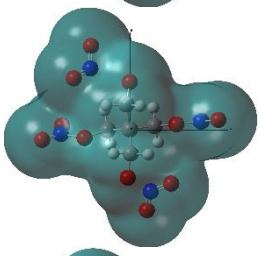
0.005	2.6×10^9	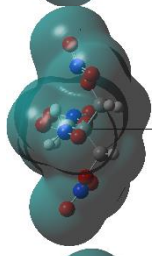	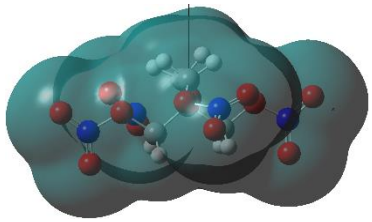	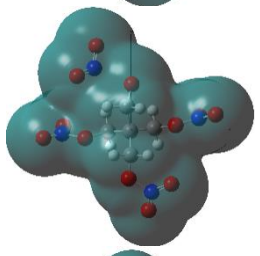
0.01	5.1×10^9	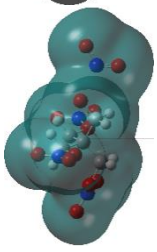	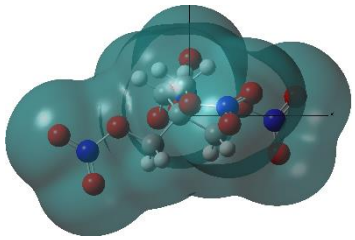	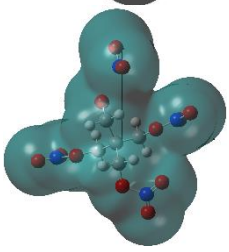

Figure 27. B3LYP-D3BJ/aug-cc-pVTZ optimized electron densities of PETN-top under an electric field applied along the y-direction viewed along x, y, and z directions. Isosurface values are 0.0004 \|e\|/Å³.

Electric Field (a.u.)	Electric Field (V/m)	View along X-direction	View along Y-direction	View along Z-direction
0	0	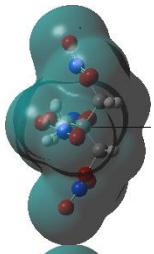	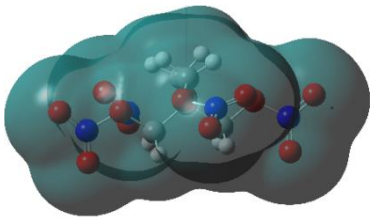	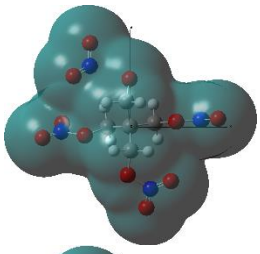
0.0001	5.1×10^7	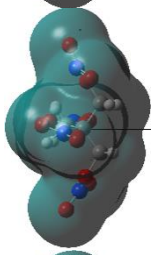	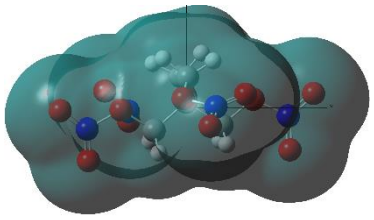	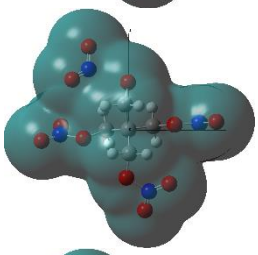
0.0005	2.6×10^8	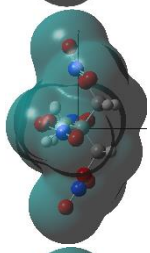	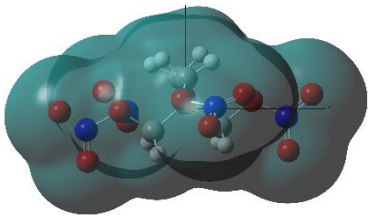	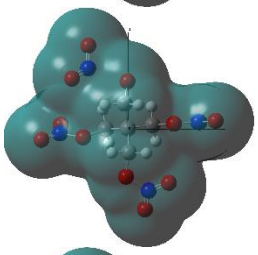
0.001	5.1×10^8	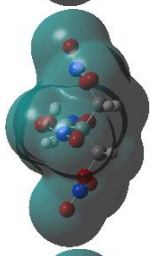	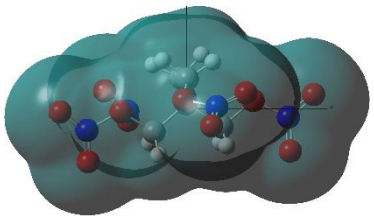	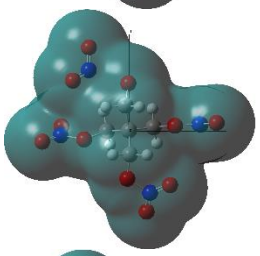
0.005	2.6×10^9	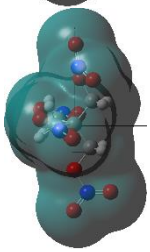	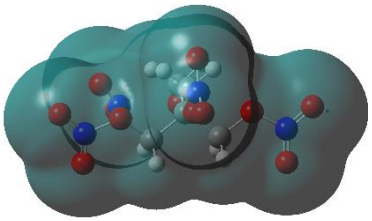	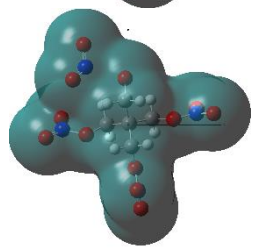

Figure 28. B3LYP-D3BJ/aug-cc-pVTZ optimized electron densities of PETN-top under an electric field applied along the z-direction viewed along x, y, and z directions. Isosurface values are 0.0004 \|e\|/Å^3.

Electric Field (a.u.)	Electric Field (V/m)	View along X-direction	View along Y-direction	View along Z-direction
0	0	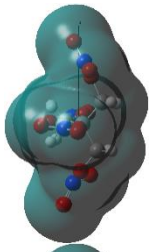	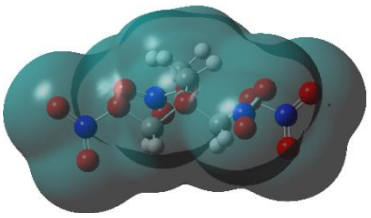	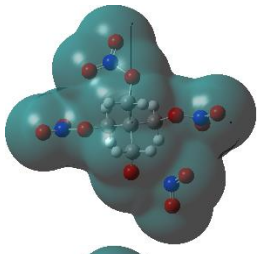
0.0001	5.1×10^7	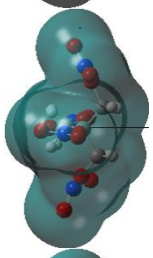	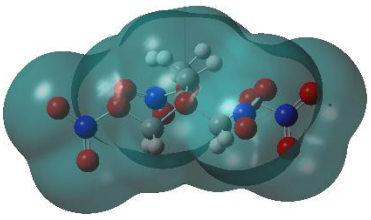	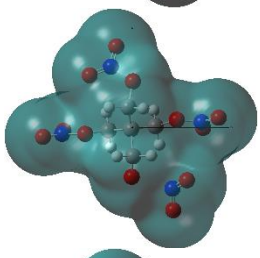
0.0005	2.6×10^8	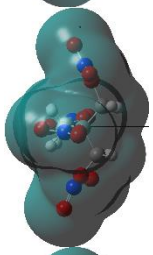	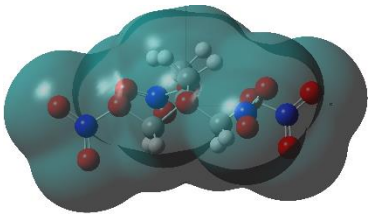	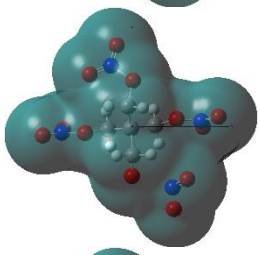
0.001	5.1×10^8	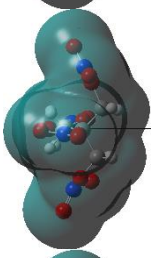	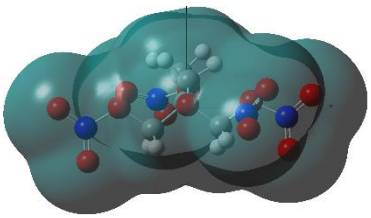	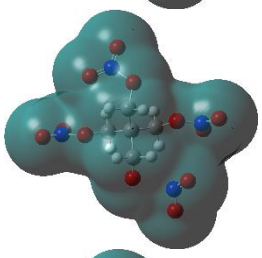
0.005	2.6×10^9	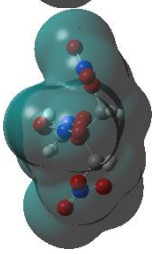	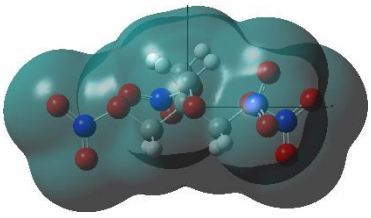	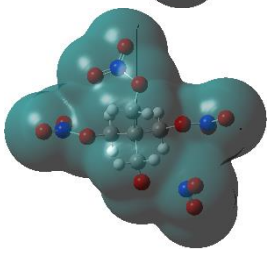

Figure 29. B3LYP-D3BJ/aug-cc-pVTZ optimized electron densities of PETN-bottom under an electric field applied along the x-direction viewed along x, y, and z directions. Isosurface values are 0.0004 \|e\|/Å^3.

Electric Field (a.u.)	Electric Field (V/m)	View along X-direction	View along Y-direction	View along Z-direction
0	0	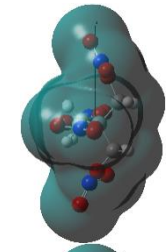	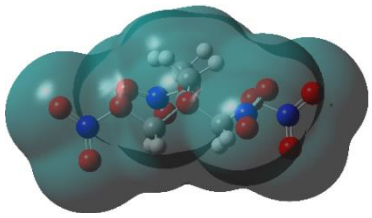	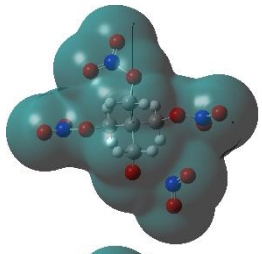
0.0001	5.1×10^7	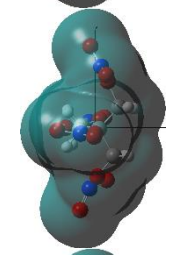	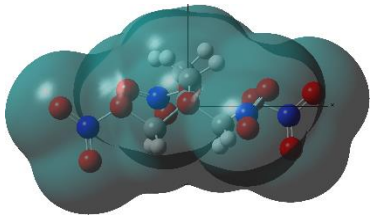	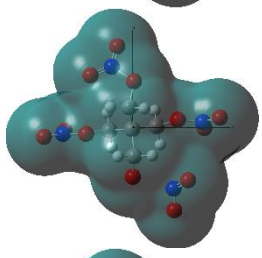
0.0005	2.6×10^8	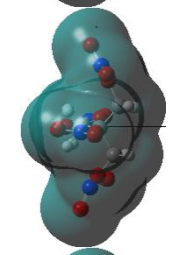	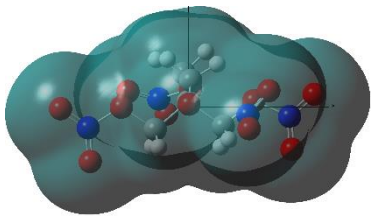	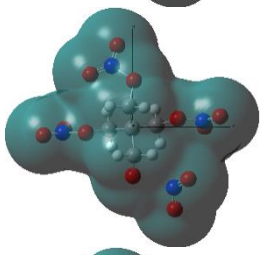
0.001	5.1×10^8	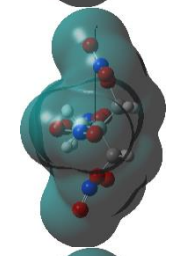	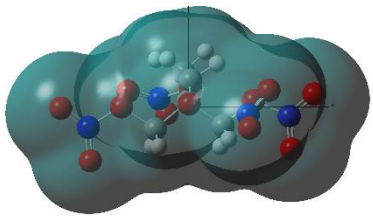	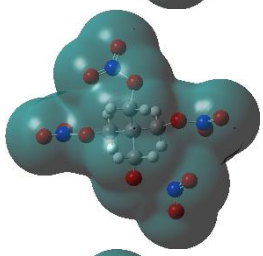
0.005	2.6×10^9	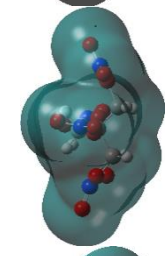	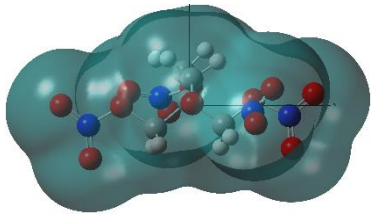	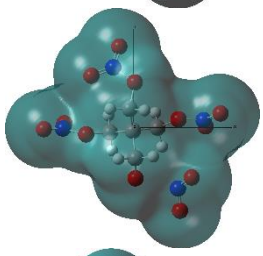
0.01	5.1×10^9	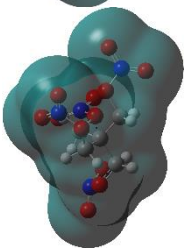	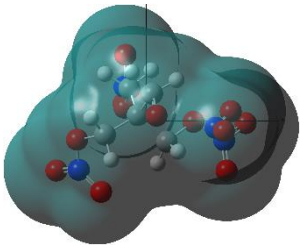	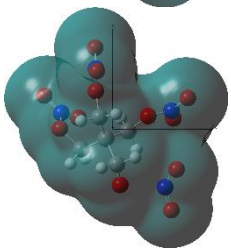

Figure 30. B3LYP-D3BJ/aug-cc-pVTZ optimized electron densities of PETN-bottom under an electric field applied along the y-direction viewed along x, y, and z directions. Isosurface values are 0.0004 \|e\|/Å^3.

Electric Field (a.u.)	Electric Field (V/m)	View along X-direction	View along Y-direction	View along Z-direction
0	0	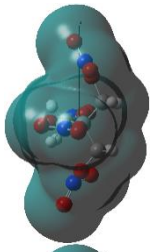	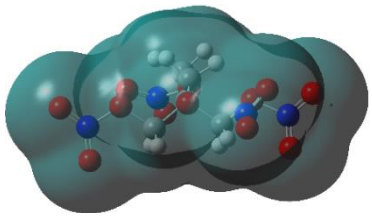	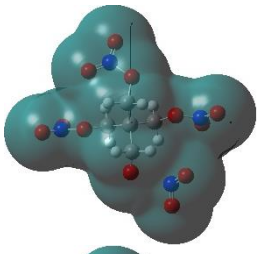
0.0001	5.1×10^7	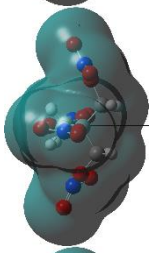	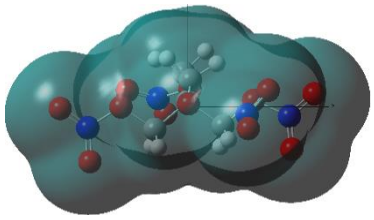	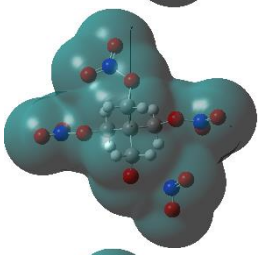
0.0005	2.6×10^8	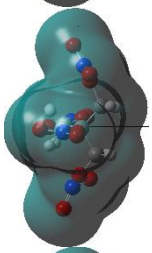	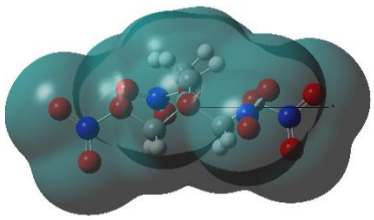	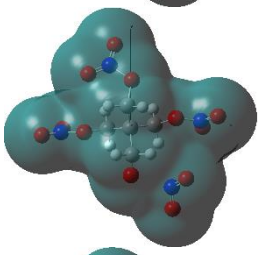
0.001	5.1×10^8	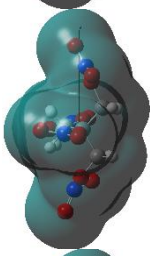	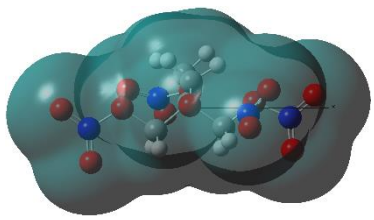	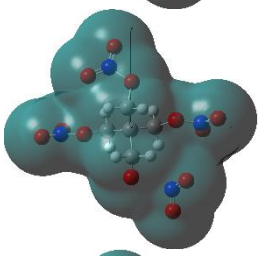
0.005	2.6×10^9	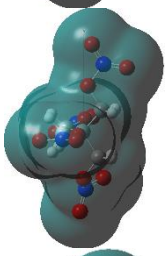	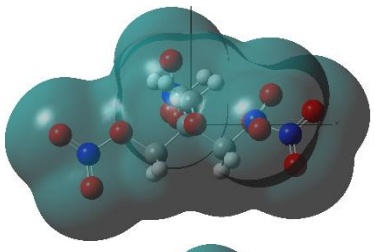	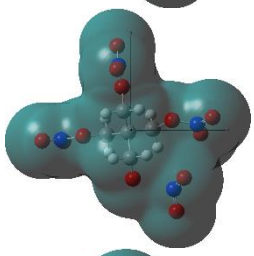
0.01	5.1×10^9	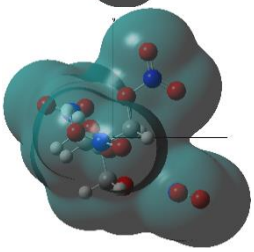	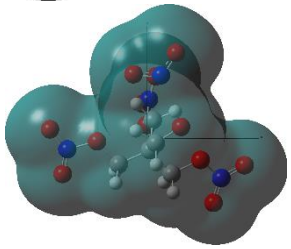	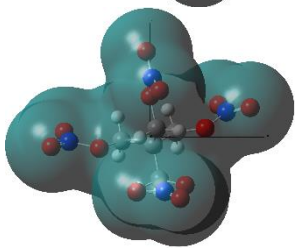

Figure 31. B3LYP-D3BJ/aug-cc-pVTZ optimized electron densities of PETN-bottom under an electric field applied along the z-direction viewed along x, y, and z directions. Isosurface values are 0.0004 |e|/Å³.

Electric Field (a.u.)	Electric Field (V/m)	View along X-direction	View along Y-direction	View along Z-direction
0	0	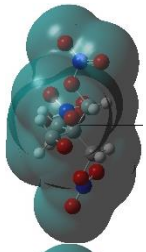	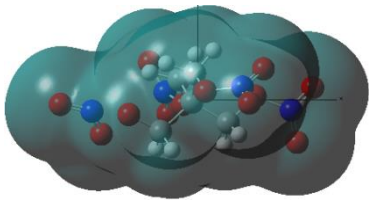	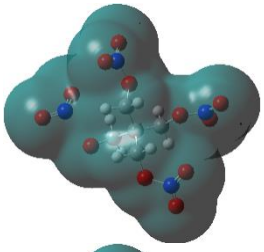
0.0001	5.1×10^7	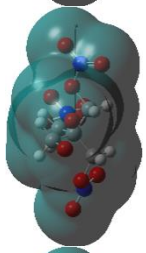	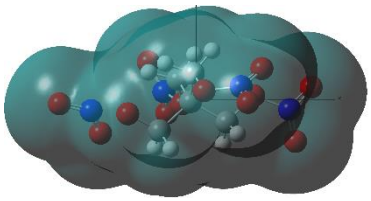	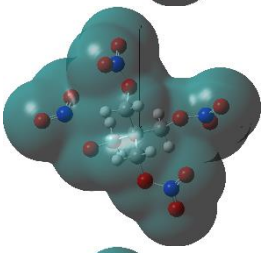
0.0005	2.6×10^8	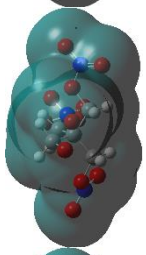	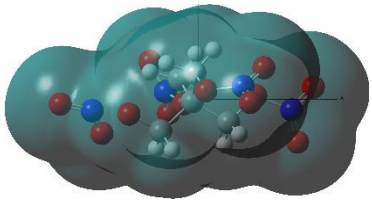	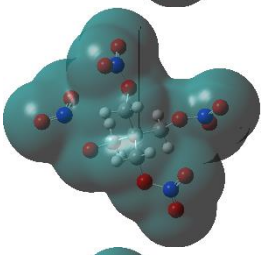
0.001	5.1×10^8	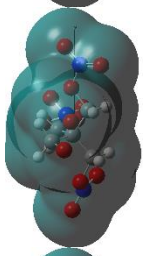	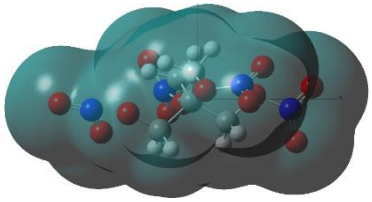	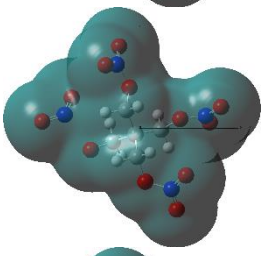
0.005	2.6×10^9	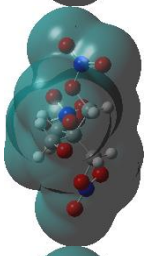	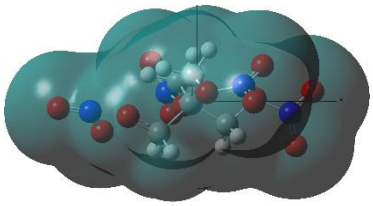	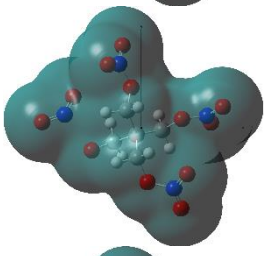
0.01	5.1×10^9	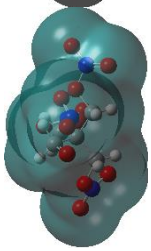	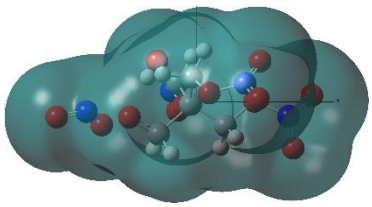	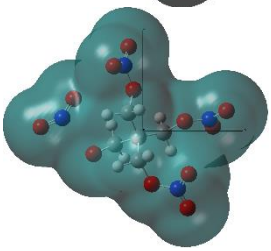

Figure 32. B3LYP-D3BJ/aug-cc-pVTZ optimized electron densities of PETN-left under an electric field applied along the x-direction viewed along x, y, and z directions. Isosurface values are 0.0004 \|e\|/Å³.

Electric Field (a.u.)	Electric Field (V/m)	View along X-direction	View along Y-direction	View along Z-direction
0	0	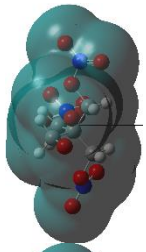	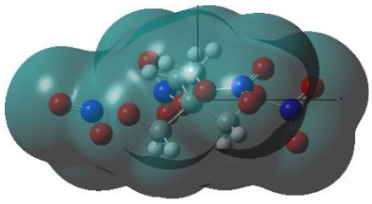	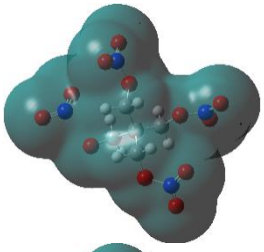
0.0001	5.1×10^7	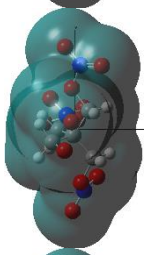	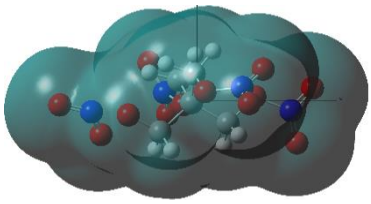	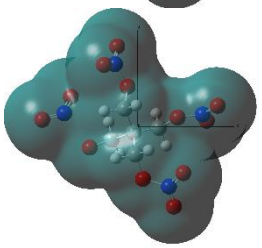
0.0005	2.6×10^8	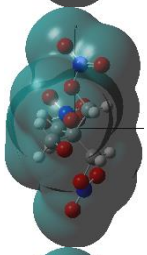	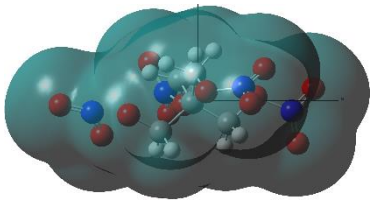	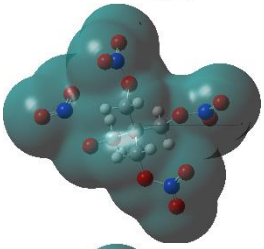
0.001	5.1×10^8	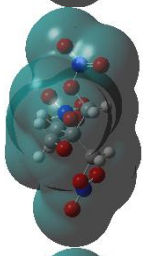	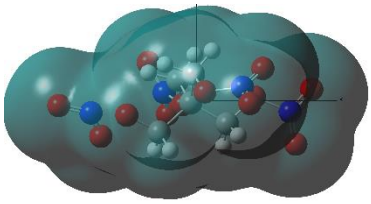	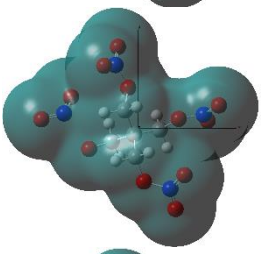
0.005	2.6×10^9	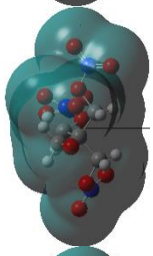	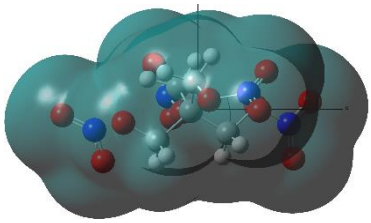	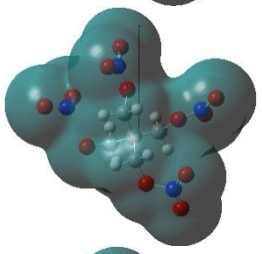
0.01	5.1×10^9	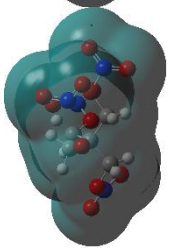	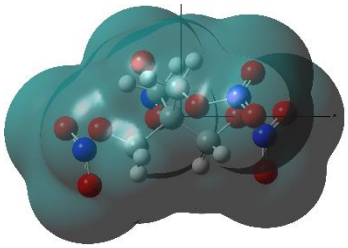	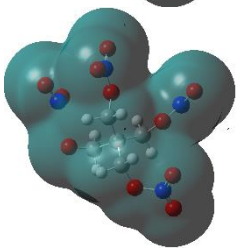

Figure 33. B3LYP-D3BJ/aug-cc-pVTZ optimized electron densities of PETN-left under an electric field applied along the y-direction viewed along x, y, and z directions. Isosurface values are 0.0004 \|e\|/Å³.

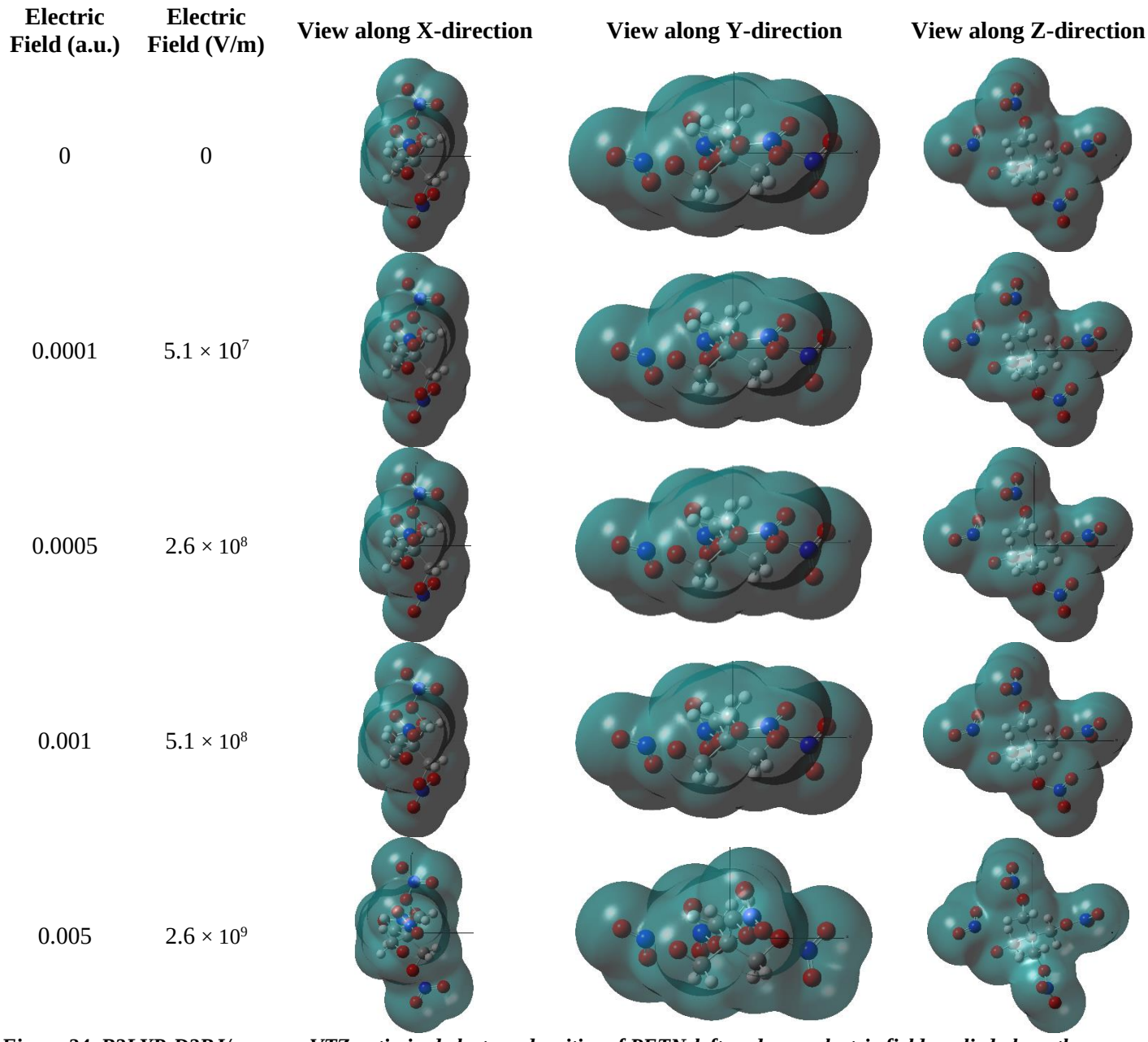

Figure 34. B3LYP-D3BJ/aug-cc-pVTZ optimized electron densities of PETN-left under an electric field applied along the z-direction viewed along x, y, and z directions. Isosurface values are 0.0004 |e|/Å³.

Electric Field (a.u.)	Electric Field (V/m)	View along X-direction	View along Y-direction	View along Z-direction
0	0	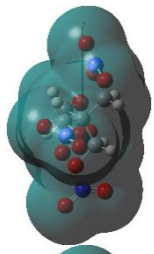	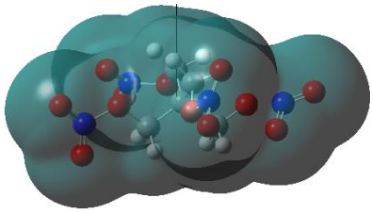	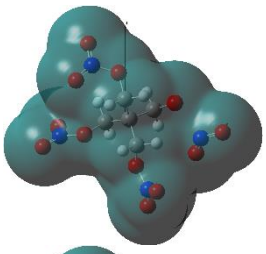
0.0001	5.1×10^7	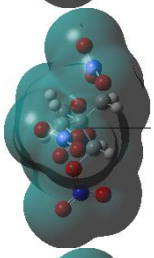	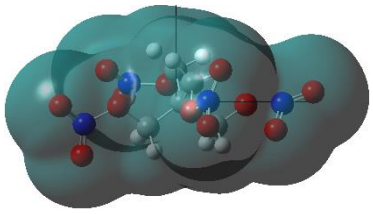	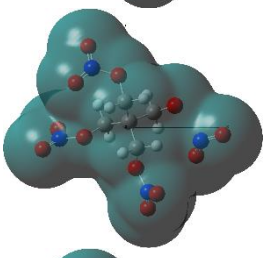
0.0005	2.6×10^8	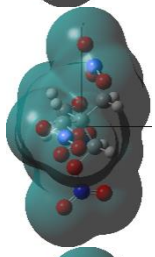	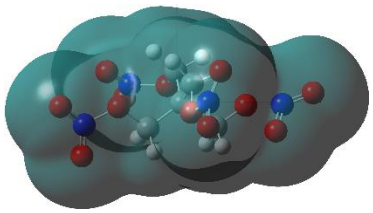	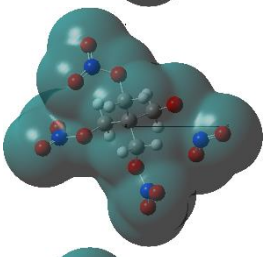
0.001	5.1×10^8	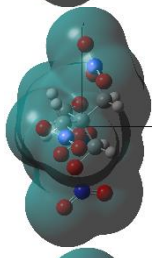	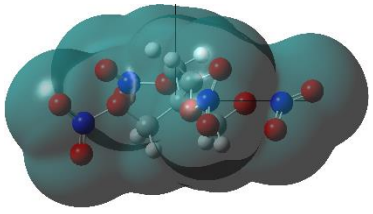	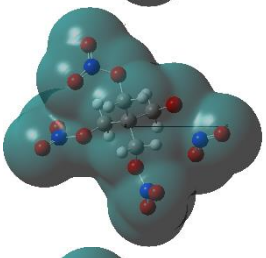
0.005	2.6×10^9	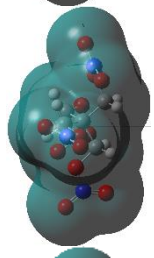	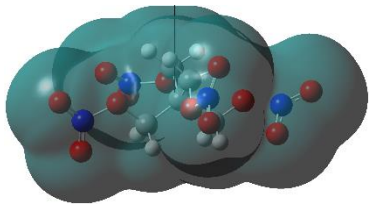	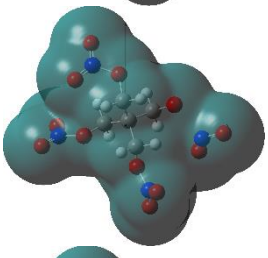
0.01	5.1×10^9	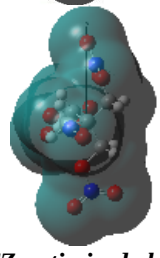	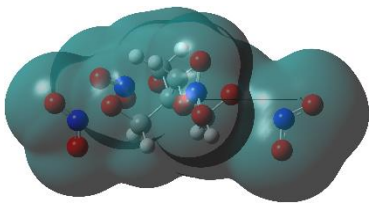	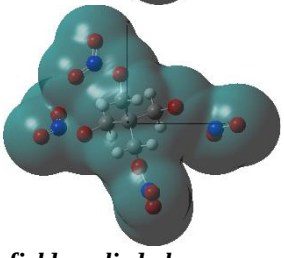

Figure 35. B3LYP-D3BJ/aug-cc-pVTZ optimized electron densities of PETN-right under an electric field applied along the x-direction viewed along x, y, and z directions. Isosurface values are 0.0004 |e|/Å³.

Electric Field (a.u.)	Electric Field (V/m)	View along X-direction	View along Y-direction	View along Z-direction
0	0	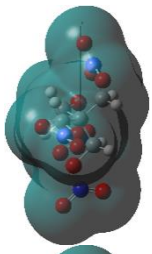	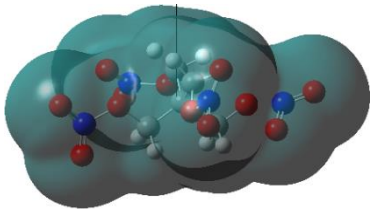	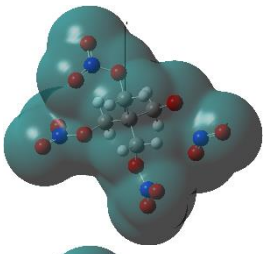
0.0001	5.1×10^7	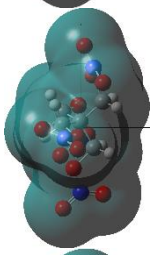	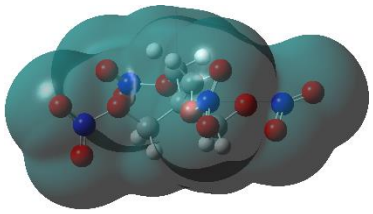	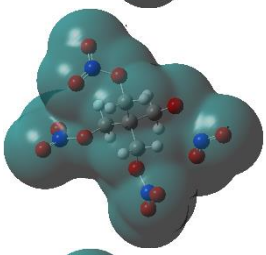
0.0005	2.6×10^8	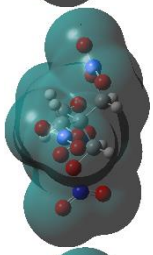	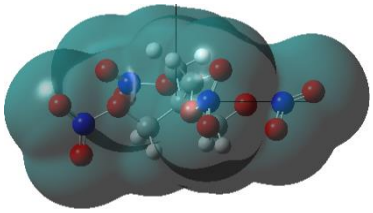	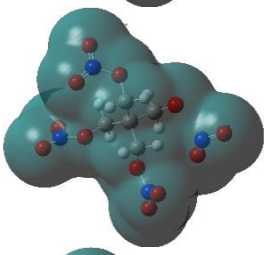
0.001	5.1×10^8	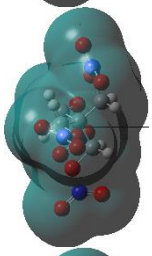	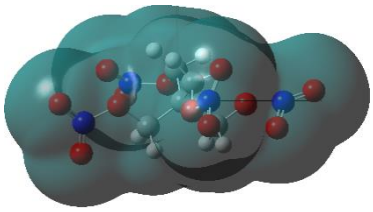	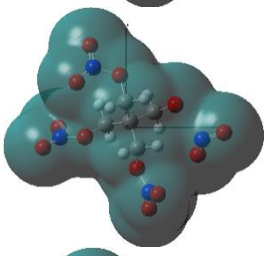
0.005	2.6×10^9	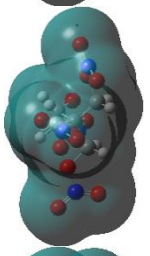	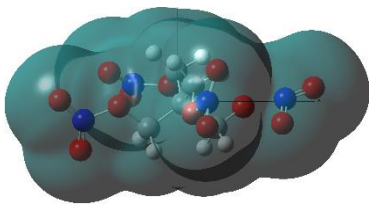	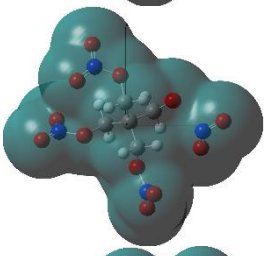
0.01	5.1×10^9	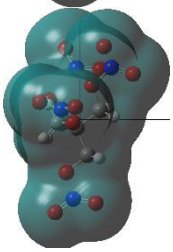	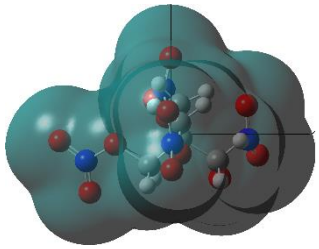	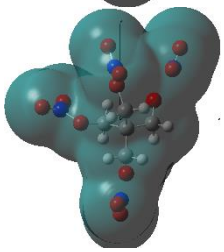

Figure 36. B3LYP-D3BJ/aug-cc-pVTZ optimized electron densities of PETN-right under an electric field applied along the y-direction viewed along x, y, and z directions. Isosurface values are 0.0004 \|e\|/Å³.

Electric Field (a.u.)	Electric Field (V/m)	View along X-direction	View along Y-direction	View along Z-direction
0	0	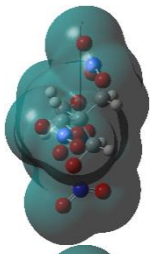	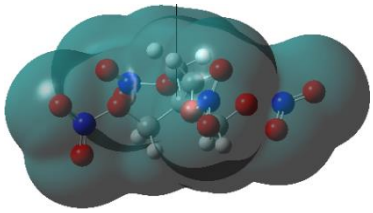	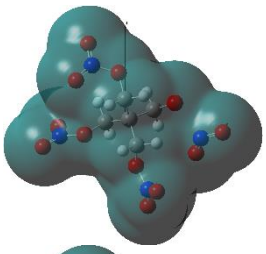
0.0001	5.1×10^7	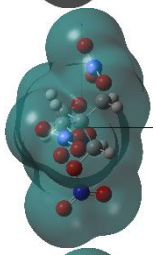	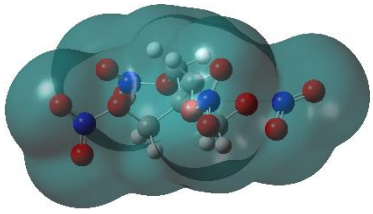	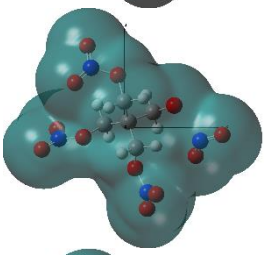
0.0005	2.6×10^8	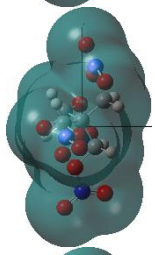	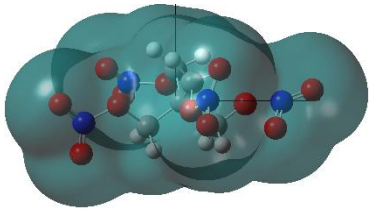	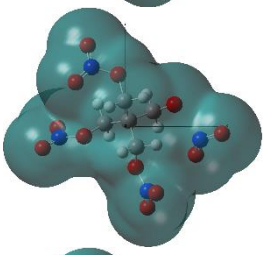
0.001	5.1×10^8	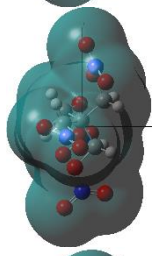	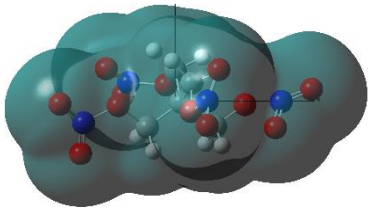	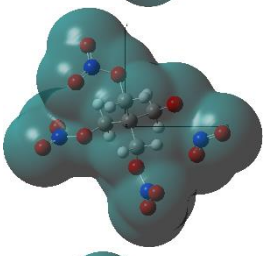
0.005	2.6×10^9	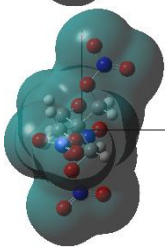	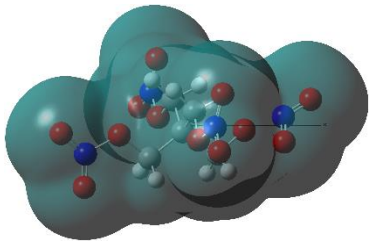	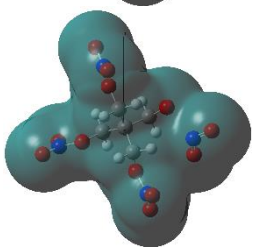

Figure 37. B3LYP-D3BJ/aug-cc-pVTZ optimized electron densities of PETN-right under an electric field applied along the z-direction viewed along x, y, and z directions. Isosurface values are 0.0004 |e|/Å^3.

Conclusions

Four high explosives were examined using density functional theory to determine how their geometry and electron density would respond to applied electric fields with varying magnitudes and orientations. The combination of the B3LYP functional with the D3BJ dispersion correction and the aug-cc-pVTZ basis set (B3LYP-D3BJ/aug-cc-pVTZ) gave good comparison to the crystal structures of RDX, TNT, and PETN, while the aug-cc-pVDZ basis set (B3LYP-D3BJ/aug-cc-pVDZ) was required for convergence of the calculations with TATB. The electric fields ranged in magnitude from 5.1×10^7 to 2.6×10^{10} V/m, which are large on the continuum scale, but are not that large on the molecular scale.

The electron densities of the HEs were anisotropic in their responses to the applied electric fields. RDX had noticeable changes to the geometry and electron density when a strong electric field was applied along the molecular x- and z-axes, but there was very little change in the geometry and electron density when the electric field was applied along the molecular y-axis. TNT behaved rather similarly to RDX, in that there were changes in geometry and electron density when an electric field was applied along the molecular x- and z-axes, but very little change occurred when the field was aligned with the molecular y-axis. PETN had noticeable changes in the geometry and electron density when the electric field was applied along each of the molecular x-, y-, and z-axes. Since TATB calculations were performed with a different basis set, the results with RDX, TNT, and PETN cannot be directly compared. The TATB calculations showed that there was not any major changes in geometry and electron density when the electric field was applied along the molecular x-axis. When electric fields had large magnitudes, like 5.1×10^9 V/m or larger, along the molecular y- and z-axes there was some twisting of the TATB molecule out of planarity, causing corresponding changes to the electron density. The trends of the dipole moments of the optimized geometries lead to two different categories: one with monotonically increasing dipole moments with increasing electric field magnitude, regardless of the orientation of the electric field and the other with one direction of electric field application leading in a decrease of the dipole moment until a large magnitude is reached, leading to an overall increased dipole moment, while the other directions have dipole moments which monotonically increase. RDX and TATB fall into the only monotonically increasing group, while PETN and TNT have one direction that decreases in dipole moment before increasing (y-axis for TNT and z-axis for PETN).

The optimized structures of the HEs with the applied electric fields were going to be used as the reactants for transition state searches to identify the transition state(s) on the path to decomposition and eventual detonation. Those transition states would then be used to calculate the activation energies under the applied electric fields. Literature searches found that the most common first step in the decomposition pathways of the 4 HEs investigated was the removal of a NO_2 group from the molecule [14-17]. To examine this, different structures were computed in which one of the nitro groups was moved further away from the rest of the molecule than in the optimized geometry. RDX, TNT, and TATB each had 3 decomposition products, while PETN had 4 products directly corresponding to the number of nitro groups in each HE. Each decomposition product structure had only one nitro group at the extended distance and the rest of the nitro groups were held at the previously optimized geometry. The R-NO_2 (R = C, N, O) distances were about 1.5 Å longer than the optimized geometries (about the same as the optimized R-N distances) and were at least 2.7 Å. These decomposition product structures were optimized without any electric fields and then the optimized structures were used as the initial estimates for the decomposition product optimizations with applied electric fields. After the geometry optimizations were completed, it was found that all of the TNT and TATB potential decomposition products optimized into structures without a free nitro group. The RDX and PETN decomposition products did have free nitro groups and analysis was performed on these structures.

The RDX decomposition products had anisotropic responses to the application of electric fields. RDX-top had ring twisting at strong magnitude electric fields aligned along the molecular x-axis and almost no changes when electric fields were aligned along the molecular y-axis. Additionally, RDX-top had a ring opening event with strong magnitude electric fields aligned along the molecular z-axis. RDX-left also had ring twisting when large magnitude electric fields were applied along the molecular x-axis, but it was relatively stable to all magnitudes of electric fields applied along the molecular y- and z-axes. RDX-right mainly had the free nitro group move in the direction of the applied electric field with very little changes in the rest of the RDX structure.

The PETN decomposition products also had anisotropic responses to the applied electric fields. When the electric field was aligned along the molecular x-axis and the magnitude was larger than 2.6×10^9 V/m, the PETN-top and PETN-right molecules turned counter-clockwise and the PETN-bottom and PETN-left did not interact much with the electric field because there were no major changes to the geometry or electron density. The PETN decomposition products all had some form of folding of the left and right nitrate ester arms towards the top nitrate ester arm under electric fields applied along the molecular y-axis. The PETN decomposition products under applied electric fields along the molecular z-axis turned counter-clockwise and one of the nitro groups twisted from parallel to the xy-plane to perpendicular to the xy-plane. Due to time constraints and computational resources, the transition state searches were not completed, but can be completed in the future to obtain the transition state geometry and the activation energy of this pathway.

Future Work

The next steps of this work are to look at larger systems of HEs and determine how they respond to electric fields. With the larger systems, the magnitude of the electric field will likely change with the system size and the effects on the molecules may also change due to intermolecular interactions and long-range ordering. By looking at more continuum-like systems, one can better understand how HEs in a larger, more realistic environment, like in propellants or explosives, will respond to external electric fields to which they might be exposed.

References

[1] Hohenberg, P.; Kohn, W. “Inhomogeneous Electron Gas” *Phys. Rev.* **1964,** *136 (3B)*, B864 - B871. DOI: 10.1103/PhysRev.136.B864

[2] Gaussian 16, Revision C.01, Frisch, M. J.; Trucks, G. W.; Schlegel, H. B.; Scuseria, G. E.; Robb, M. A.; Cheeseman, J. R.; Scalmani, G.; Barone, V.; Petersson, G. A.; Nakatsuji, H.; Li, X.; Caricato, M.; Marenich, A. V.; Bloino, J.; Janesko, B. G.; Gomperts, R.; Mennucci, B.; Hratchian, H. P.; Ortiz, J. V.; Izmaylov, A. F.; Sonnenberg, J. L.; Williams-Young, D.; Ding, F.; Lipparini, F.; Egidi, F.; Goings, J.; Peng, B.; Petrone, A.; Henderson, T.; Ranasinghe, D.; Zakrzewski, V. G.; Gao, J.; Rega, N.; Zheng, G.; Liang, W.; Hada, M.; Ehara, M.; Toyota, K.; Fukuda, R.; Hasegawa, J.; Ishida, M.; Nakajima, T.; Honda, Y.; Kitao, O.; Nakai, H.; Vreven, T.; Throssell, K.; Montgomery, J. A., Jr.; Peralta, J. E.; Ogliaro, F.; Bearpark, M. J.; Heyd, J. J.; Brothers, E. N.; Kudin, K. N.; Staroverov, V. N.; Keith, T. A.; Kobayashi, R.; Normand, J.; Raghavachari, K.; Rendell, A. P.; Burant, J. C.; Iyengar, S. S.; Tomasi, J.; Cossi, M.; Millam, J. M.; Klene, M.; Adamo, C.; Cammi, R.; Ochterski, J. W.; Martin, R. L.; Morokuma, K.; Farkas, O.; Foresman, J. B.; Fox, D. J. Gaussian, Inc., Wallingford CT, 2016.

[3] GaussView, Version 6, Dennington, R.; Keith, T. A.; Millam, J. M. Semichem Inc., Shawnee Mission, KS, 2016.

[4] Stephens, P. J.; Devlin, F. J.; Chabalowski, C. F.; Frisch, M. J. "Ab Initio Calculation of Vibrational Absorption and Circular Dichroism Spectra Using Density Functional Force Fields." J. Phys. Chem. **1994**, *98 (45)*, 11623-11627. DOI: 10.1021/j100096a001

[5] Grimme, S.; Ehrlich, S.; Goerigk, L. “Effect of the damping function in dispersion corrected density functional theory” *J. Comp. Chem.* **2011**, *32 (7)*, 1456 - 1465. DOI: 10.1002/jcc.21759

[6] Kendall, R. A.; Dunning Jr., T. H.; Harrison, R. J. “Electron affinities of the first-row atoms revisited. Systematic basis sets and wave functions,” *J. Chem. Phys.*, **1992**, *96*, 6796-6806. DOI: 10.1063/1.462569

[7] Lee, R. J. *STATIC DIELECTRIC BREAKDOWN STRENGTH OF CONDENSED HETEROGENEOUS HIGH EXPLOSIVES*; Technical Report No. 85-380 for Naval Surface Weapons Center: Silver Spring, MD, June 1987.

[8] Zachariah, M. R. *Fundamental Reactive Characterization of Novel Nano-Scale Assembled Fuel/Oxidizers Using a New Mass-Spectrometry T-Jump Approach*; Technical Report No. HDTRA1-07-1-0020 for Defense Threat Reduction Agency: Ft. Belvoir, VA, March 2014.

[9] Choi, C. S.; Prince, E. "The Crystal Structure of Cyclotrimethylene-trinitramine" *Acta. Cryst.* **1972**, *B28*, 2857-2862 DOI: 10.1107/S0567740872007046

[10] Gallagher, H. G.; Roberts, K. J.; Sherwood, J. N.; Smith, L. A. "A theoretical examination of the molecular packing, intermolecular bonding and crystal morphology of 2,4,6-trinitrotoluene in relation to polymorphic structural stability" *J. Mater. Chem.* **1997**, *7(2)*, 229-235. DOI: 10.1039/A603983I

[11] Cady, H. H.; Larson, A. C. "The Crystal Structure of 1,3,5-Triamino-2,4,6-trinitrobenzene" *Acta Cryst.* **1965**, *18*, 485-496. DOI: 10.1107/S0365110X6500107X

[12] Cady, H, H.; Larson, A. C. "Pentaerythritol Tetranitrate II: Its Crystal Structure and Transformation to PETN I; an Algorithm for Refinement of Crystal Structures with Poor Data" *Acta Cryst.* **1975**, *B31*, 1864-1869. DOI: 10.1107/S0567740875006383

[13] Computational Chemistry Comparison and Benchmark Database, release 22 (May 2022); Standard Reference Database 101; National Institute of Standards and Technology. https://cccbdb.nist.gov/diplistx.asp#NISTdiatomic (Accessed on 15 August 2022).

[14] Chakraborty, D.; Muller, R. P.; Dasgupta, S.; Goddard III, W. A.; "The Mechanism for Unimolecular Decomposition of RDX (1,3,5-Trinitro-1,3,5-triazine), an ab Initio Study" *J. Phys. Chem. A*, **2000**, *104*, 2261-2272. DOI: 10.1021/jp9936953

[15] Rom, N.; Hirshberg, B.; Zeiri, Y.; Furman, D.; Zybin, S. V.; Goddard III, W. A.; Kosloff, R. "First-Principles-Based Reaction Kinetics for Decomposition of Hot, Dense Liquid TNT from ReaxFF Multiscale Dynamics Simulations" *J. Phys. Chem. C* **2013**, *117*, 21043-21054. DOI: 10.1021/jp404907b

[16] He, Z.-H.; Yu, Y.; Huang, Y.-Y.; Chen, J.; Wu, Q. "Reaction kinetic properties of 1,3,5-triamino-2,4,6-trinitrobenzene: a DFTB study of thermal decomposition" *New J. Chem.* **2019**, *43*, 18027-18033. DOI: 10.1039/C9NJ04340C

[17] Pouretedal, H. R.; Damiri, S.; Ravanbod, M.; Haghdost, M.; Masoudi, S. "The kinetic of thermal decomposition of PETN, Pentastite and Pentolite by TG/DTA non-isothermal methods" *J. Therm. Anal. Calorim.* **2017**, *129*, 521-529. DOI: 10.1007/s10973-017-6164-0

DISTRIBUTION

Internal:

ALBERT T CAMP TECHNICAL LIBRARY
4171 FOWLER ROAD SUITE 101
INDIAN HEAD, MD 20640-5110 1

Electronic Copy:

ADMINISTRATOR
DEFENSE TECH INFORMATION CTR
ATTN JACK RIKE OCA
8725 JOHN J KINGMAN RD STE 0944
FT BELVOIR VA 22060-6218

This page intentionally left blank.